SAND2016-8697R

International Collaboration on Used Fuel Disposition Crystalline Rocks: FY16 Progress Report

Fuel Cycle Research & Development

Prepared for
U.S. Department of Energy
Used Fuel Disposition
Yifeng Wang
Sandia National Laboratories
Payton Gardner
University of Montana
Geon-Young Kim, Sung-Hoon Ji
Korean Atomic Energy Research Institute
August 26, 2016
FCRD-UFD-2016-000629

Sandia National Laboratories is a multi-program laboratory managed and operated by Sandia Corporation, a wholly owned subsidiary of Lockheed Martin Corporation, for the U.S. Department of Energy's National Nuclear Security Administration under contract DE-AC04-94AL85000.

FCT Quality Assurance Program Document

Appendix E
FCT Document Cover Sheet

Name/Title of Deliverable/Milestone	International collaboration on used fuel disposition in crystalline rocks: FY16 progress report (M4FT-16SN080303091)
Work Package Title and Number	Crystalline Disposal R&D (International)
Work Package WBS Number	FT-16SN08030309
Responsible Work Package Manager	Yifeng Wang (Name/Signature)

Date Submitted 8/26/2016

Quality Rigor Level for Deliverable/Milestone	☐ QRL-3	☐ QRL-2	☐ QRL-1 ☐ Nuclear Data	☒ N/A*

This deliverable was prepared in accordance with Sandia National Laboratories
(Participant/National Laboratory Name)

QA program which meets the requirements of
☒ DOE Order 414.1 ☐ NQA-1-2000

This Deliverable was subjected to:

☐ Technical Review

Technical Review (TR)

Review Documentation Provided

☐ Signed TR Report or,
☐ Signed TR Concurrence Sheet or,
☐ Signature of TR Reviewer(s) below

Name and Signature of Reviewers

N/A

☐ Peer Review

Peer Review (PR)

Review Documentation Provided

☐ Signed PR Report or,
☐ Signed PR Concurrence Sheet or,
☐ Signature of PR Reviewer(s) below

*Note: In some cases there may be a milestone where an item is being fabricated, maintenance is being performed on a facility, or a document is being issued through a formal document control process where it specifically calls out a formal review of the document. In these cases, documentation (e.g., inspection report, maintenance request, work planning package documentation or the documented review of the issued document through the document control process) of the completion of the activity along with the Document Cover Sheet is sufficient to demonstrate achieving the milestone. QRL for such milestones may be also be marked N/A in the work package provided the work package clearly specifies the requirement to use the Document Cover Sheet and provide supporting documentation.

USED FUEL DISPOSITION IN CRYSTALLINE ROCKS: FY16 PROGRESS REPORT

EXECUTIVE SUMMARY

Active participation in international R&D is crucial for achieving the UFD long-term goals of conducting "experiments to fill data needs and confirm advanced modeling approaches" (by 2015) and of having a "robust modeling and experimental basis for evaluation of multiple disposal system options" (by 2020). DOE's Office of Nuclear Energy (NE) and its Office of Used Fuel Disposition Research and Development (UFD) have developed a strategic plan to advance cooperation with international partners. The international collaboration on the evaluation of crystalline disposal media at Sandia National Laboratories (SNL) in FY16 focused on the following four activities: (1) thermal-hydrologic-mechanical-chemical modeling single fracture evolution; (2) simulations of flow and transport in Bedrichov Tunnel, Czech Republic, (3) completion of streaming potential testing at Korean Atomic Energy Research Institute (KAERI), and (4) technical data exchange with KAERI on thermal-hydrologic-mechanical (THM) properties and specifications of bentonite buffer materials. The first two activities are part of the Development of Coupled Models and their Validation against Experiments (DECOVALEX-2015) project. The major accomplishments include:

- *DECOVALEX C.1: Thermal-Hydrologic-Mechanical-Chemical (THMC) Processes in Single Fractures:* Understanding of subsurface fracture opening and closure is of great importance to oil/gas production, geothermal energy extraction, radioactive waste disposal, and carbon sequestration and storage. Fracture opening and closure involve a complex set of thermal, hydrologic, mechanical and chemical (THMC) processes. A fully coupled THMC model for fracture opening and closure is formulated by explicitly accounting for the stress concentration on aperture surface, stress-activated mineral dissolution, pressure solution at contacting asperities, and channel flow dynamics. A model analysis, together with reported laboratory observations, shows that a tangential surface stress created by a far-field compressive normal stress may play an important role in controlling fracture aperture evolution in a stressed geologic medium, a mechanism that has not been considered in any existing models. Based on the model analysis, a necessary condition for aperture opening has been derived. The model provides a reasonable explanation for many salient features of fracture evolution in laboratory experiments, including a spontaneous switch from a permeability reduction to a permeability increase in a static limestone experiment. The work may also help develop a new method for estimating in-situ stress in a reservoir.
- *DECOVALEX C.2: Bedrichov Tunnel Test Case:* The transit time distribution (TTD) of discharge collected from fractures in the Bedrichov Tunnel, Czech Republic, is investigated using lumped parameter models and multiple environmental tracers. We utilize time series of $\delta^{18}O$, $\delta^{2}H$ and $\delta^{3}H$ along with CFC measurements from individual fractures in the Bedrichov Tunnel of the Czech Republic to investigate the TTD, and the uncertainty in estimated mean travel time in several fracture networks of varying length and discharge. We compare several transit time distributions, including the dispersion distribution, the exponential distribution, and a developed TTD which includes the effects of matrix diffusion. The effect of seasonal recharge is explored by

comparing several seasonal weighting functions to derive the historical recharge concentration. We identify best fit mean ages for each TTD by minimizing the error-weighted, multi-tracer χ^2 residual for each seasonal weighting function. We use this methodology to test the ability of each TTD and seasonal input function to fit the observed tracer concentrations, and the effect of choosing different TTD and seasonal recharge functions on the mean age estimation. We find that the estimated mean transit time is a function of both the assumed transit time distribution and seasonal weighting function. Best fits as measured by the χ^2 value were achieved for the dispersive model using the seasonal input function developed here for two of the three modeled sites, while at the third site, equally good fits were achieved with the exponential model and the dispersion model and our seasonal input function. The average mean transit time for all TTDs and seasonal input functions converged to similar values at each location. The sensitivity of the estimated mean transit time to the seasonal weighting function was equal to that of the transit time distribution. These results indicated that understanding seasonality of recharge is at least as important as the uncertainty in the flow path distribution in fracture networks, and that unique identification of the TTD and mean transit time is difficult given the uncertainty in the recharge function. However, the mean transit time appears to be relatively robust to the structural model uncertainty. The results presented here should be applicable to other studies using environmental tracers to constrain ow and transport properties in fractured rock systems.

- *Collaboration with KAERI:* SNL and KAERI have developed a multi-year plan for joint field testing and modeling to support the study of high-level nuclear waste disposal in crystalline geologic media. In FY16, KAERI completed the task on streaming potential (SP) testing and initiated a new task on technique development for in-situ borehole characterization. The new task is a jointed effort between the UFD deep borehole disposal work package and the crystalline disposal R&D work package. In FY16, KAERI also provided the data on THM properties and specifications of bentonite buffer materials. For the streaming potential testing, a sandbox experiment was established at KAERI to study the hydroelectric coupling. An acrylic tank was filled up with homogeneous sand as a sand aquifer, and the upstream and downstream reservoirs were connected to the sand aquifer to control the hydraulic gradient. Under a steady-state water flow condition, a tracer test was performed in the sandbox with the help of peristaltic pump, and tracer samples were collected from the same interval of five screened wells in the sandbox. During the tracer test, SP signals resulting from the distribution of 20 nonpolarizable electrodes were measured at the top of the tank by a multichannel meter. The results showed that there were changes in the observed SP after injection of tracer, which indicated that the SP was likely to be related to the solute transport.

Future work will include: (1) developing a plan for the participation in the new phase of the DECOVALEX project, (2) initiating an actual field test at the KURT site for the development of in-situ measurement techniques in boreholes, and (3) using the data obtained from the international collaboration for UFD model validation and demonstration.

CONTENTS

1. OBJECTIVES

Recognizing the benefits of international collaboration in the common goal of safely and efficiently managing the back end of the nuclear fuel cycle, DOE's Office of Nuclear Energy (NE) and its Office of Used Fuel Disposition Research and Development (UFD) have developed a strategic plan to advance cooperation with international partners (Birkholzer et al., 2013; UFD, 2012). UFD's strategic plan lays out two interdependent areas of international collaboration. The first area is cooperation with the international nuclear community through participation in international organizations, working groups, committees, and expert panels. Such participation typically involves conference and workshop visits, information exchanges, reviews, and training and education. The second area of international collaboration is active R&D participation of U.S. researchers within international projects or programs (UFD, 2012). By active R&D, it is meant that U.S. researchers work closely together with international scientists on specific R&D projects relevant to both sides. With respect to geologic disposal of radioactive waste, such active collaboration provides direct access to information, data, and expertise on various disposal options and geologic environments that have been collected internationally over the past decades. Many international programs have operating underground research laboratories (URLs) in clay/shale, granite, and salt environments, in which relevant field experiments have been and are being conducted. Depending on the type of collaboration, U.S. researchers can participate in planning, conducting, and interpreting experiments in these URLs, and thereby get early access to field studies without having in situ research facilities in the United States.

UFD considers this second area, active international R&D, to be very beneficial in achieving the program's long-term goals of conducting "experiments to fill data needs and confirm advanced modeling approaches" (by 2015) and of having a "robust modeling and experimental basis for evaluation of multiple disposal system options" (by 2020). Advancing opportunities for active international collaboration with respect to geologic disposal has therefore been the primary focus of UFD's international strategy in the recent year (Birkholzer et al., 2013; Birkholzer, 2012).

This report summarizes the work accomplished in FY16 at Sandia National Laboratories (SNL) related to international collaborations on the evaluation of crystalline rocks as disposal media. The FY15 work was focused on the the following three activities: (1) thermal-hydrologic-mechanical-chemical modeling single fracture evolution; (2) simulations of flow and transport in Bedrichov Tunnel, Czech Republic, (3) streaming potential testing at Korean Atomic Energy Research Institute (KAERI), and (4) technical data exchange with KAERI on thermal-hydrologic-mechanical (THM) properties and specifications of bentonite buffer materials. The first two activities are part of the Development of Coupled Models and their Validation against Experiments (DECOVALEX-2015) project. This work directly supports the following UFD objectives:

- Develop a fundamental understanding of disposal system performance in a range of environments for potential wastes that could arise from future nuclear fuel cycle alternatives through theory, simulation, testing, and experimentation.
- Develop a computational modeling capability for the performance of storage and disposal options for a range of fuel cycle alternatives, evolving from generic models to more robust models of performance assessment.

The work documented here also addresses the following specific topics identified based on the UFD R&D Implementation Plan (Wang, 2014).

- Topic #S5: Evaluation of state of the art of site characterization techniques
- Topic #S7: Identification of the needs for using underground research laboratory
- Topic #P1: Development of discrete fracture network model
- Topic #P2: Parameter estimation and uncertainty quantification of field testing

1.1 REFERENCES

Birkholzer, J.T. (2012). Status of UFD Campaign International Activities in Disposal Research. Report prepared for U.S. Department of Energy Used Fuel Disposition Campaign, FCRD-UFD-2012-000295.

Birkholzer, J., Asahina, D., Chen, F., Gardner, P., Houseworth, J., Jove-Colon, C., Kersting, A., Nair, P., Nutt, M., Li, L., Liu, H.H., Painter, S., Reimus, P., Rutqvist, J., Steefel, C., Tynan, M., Wang, Y., Zavarin, M. (2013). An overview of US disposal research activities linked to international URLs. Proceedings of the 2013 International High-Level Radioactive Waste Management Conference (IHLRWM), April 28 – May 2, 2013, Albuquerque, New Mexico.

UFD (2012). Office of Used Fuel Disposition International Program — Strategic Plan (2013) April 2012, U.S. Department of Energy.

Wang, Y. (2014) Used Fuel Disposal in Crystalline Rocks: Status and FY14 Progress, FCRD-UFD-2014-000060.

2. THERMAL-HYDROLOGIC-MECHANICAL-CHEMCIAL MOLDEING OF SUBSURFACE FRACTURE OPENING AND CLOSURE

2.1 INTRODUCTION

Understanding of fracture opening and closure in geologic media is crucial for oil/gas production, geothermal energy extraction, radioactive waste disposal, and carbon sequestration and storage (e.g., Yasuhara et al., 2006; Ellis et al., 2013). It has been observed that, under certain circumstances, a fracture can undergo either opening or closure or switch from one regime to another (Polak et al., 2004; Liu et al., 2006; McGuire et al., 2013). Fracture evolution involves a complex set of coupled physical and chemical processes, including stress-mediated mineral dissolution/precipitation, fluid flow and transport, mechanical deformation, etc. Significant effort has been made to understand these processes in laboratories. For example, in a flow-through experiment on a natural novaculite fracture under moderate effective stress (~14 bars), Yasuhara et al. (2006) observed a reduction in fracture permeability for the first 1500 hours followed by a significant increase in fracture aperture as the fluid flow rate and the temperature in the experiment were ramped up. In a similar experiment on a limestone fracture, Polak et al. (2004) observed that, during the initial circulation of groundwater, the differential pressure increased about threefold as the contacting asperities across the fracture were removed. Interestingly, after switching to distilled water, they first observed another threefold reduction in permeability and then a spontaneous switch from a permeability reduction to a permeability increase without any change in experimental conditions. The underlying mechanism for this switch is unknown. An increase in permeability usually involves preferential dissolution channeling (Elkhoury et al., 2013).

Various models have been developed for fracture opening and closure, with various levels of complexity with respect to process couplings, ranging from a simple geometrical model to a coupled thermal-hydrologic-mechanical-chemical (THMC) model (Table 1). However, those models are to a large extent empirical and thus not amenable for predictions. No existing model is able to provide a consistent explanation for some key features of fracture evolution often observed in laboratory experiments, for example, a spontaneous transition from a permeability reduction to a permeability increase (Polak et al., 2004), an enhancement of fracture permeability by temperature (Yasuhara et a., 2006), or a similar enhancement by a low-pH solution (McGuire et al., 2013). Questions, such as what role a normal stress would play in fracture evolution and under what conditions a fracture would tend to open or close, still remain open.

The objective of this section is to lay a theoretical foundation for modeling subsurface fracture opening and closure. The model proposed below is a fully coupled THMC model that explicitly accounts for three key processes: (1) stress concentration around individual aperture channels, (2) stress-activated mineral dissolution on fracture surfaces, and (3) reactive infiltration instability of fluid flow in fracture aperture. This model is based on a recent observation in materials science that a tangential surface stress may enhance or inhibit mineral reaction on a stressed solid surface (Aziz et al., 1991; Yu and Suo, 2000). The work presented here will for

the first time demonstrate that this mechanism may also play an important role in fracture aperture evolution in a stressed geologic medium. Based on a model analysis, a necessary condition for aperture opening will be derived. The proposed model will be able to explain key features of fracture evolution often observed in laboratory experiments. The geologic implications of the model results will also be discussed

2.2 MODEL FORMULATION

Geometric representation of a single fracture

It is assumed that a fracture plane can be represented with stripes of contacting areas (asperities) surrounded by aperture channels (Fig. 1). It is further assumed that the cross section of an individual aperture channel can be described by a truncated ellipse defined by the intersection of two identical ellipses (Fig. 2):

$$\frac{x\prime^2}{a\prime^2}+\frac{(y'-h)^2}{b\prime^2}=1 \quad (1)$$

$$\frac{x\prime^2}{a\prime^2}+\frac{(y'+h)^2}{b\prime^2}=1 \quad (2)$$

where *x'* and *y'* are the local coordinates; and *a'* and *b'* are the major and minor semi-axes of the two intersecting ellipses respectively. Parameters *a'* and *b'* are related to the semi-axes of the truncated ellipse (*a*, *b*) by (Fig. 2):

$$a'=\frac{h+b}{\sqrt{(h+b)^2-h^2}}a \quad (3)$$

$$b'=h+b. \quad (4)$$

The area of the cross section (*S*) can be calculated by:

$$S=1a'b'\arcsin\left(\frac{a}{a'}\right)-2ha \quad (5)$$

The contact area ratio of a fracture can then be defined by:

$$f_c=1-\alpha\sqrt{1-\left(1-\frac{b}{b'}\right)^2} \quad (6)$$

with

$$\alpha=\frac{a'}{a_0+g_0}$$

where a_0 and e_0 are the initial widths of the aperture channel (*a*) and the neighboring contacting asperities (*g*) respectively. As shown in Fig. 3, Equation (6) is able to fit the measured aperture-contact area relation relatively well, indicating that the geometry of an actual aperture channel

can be represented adequately by a truncated ellipse. This is certainly an advantage over other geometrical representations such as a triangular channel (Liu et al., 2006), which are usually not able to reproduce the measured relationship.

Local stresses

The model proposed here explicitly accounts for the stress concentration at a fracture contact area and on the surface of an aperture channel under a far-field compressive normal stress (σ_∞) (Fig. 1). To simplify stress-concentration calculations, it is assumed that the geometry of a truncated elliptic channel can still be approximated by a normal ellipse with the same semi-axes. The stress at any point of fracture surface can be split into two orthogonal components: the normal stress (perpendicular to the surface) and the tangential stress (parallel to the surface) (Chung and Fuller, 1992).

Adopting a convention of a compressive stress being positive, we have at a fracture contact:

$$\sigma_\infty = p_f(1 - f_c) + \sigma_c^n f_c \tag{7}$$

$$\sigma_c^t = p_f \tag{8}$$

where p_f is the pore fluid pressure; σ_c^n and σ_c^t are the normal and tangential stresses at the contact respectively. Similarly, on an aperture channel surface, we have (Reuschlé et al., 1988):

$$\sigma_p^n = p_f \tag{9}$$

$$\sigma_p^t(\theta) = p_f - \frac{(1-m^2)(-\sigma_\infty+2p_f)+2\sigma_\infty(m-cos2\theta)}{1+m^2-2mcos2\theta} \tag{10}$$

where $m = (a-b)/(a+b)$; σ_p^n and σ_p^t are the normal and tangential stresses on the surface; and θ is the eccentric angle of the point under consideration on the aperture surface (Fig. 1A).

Strain energy

The elastic strain energy at a specific point of a fracture surface is estimated to be on the order of $\frac{\sigma^2}{2E}$, where σ is the stress exerted at that point and E is the Young's modulus of the rock involved (Reuschlé et al., 1988). This energy is usually small and can be negligible (Bruton and Helgeson, 1983). Other processes may also contribute to the total strain energy of a stressed rock, such as a strain energy arising from lattice mismatches along grain boundaries (Wang and Vitek, 1986) and an additional energy resulted from the formation of various defects and dislocations within stressed crystals (Shimizu, 1995). We assume that the total strain energy at a specific point of a fracture surface is quadratically proportional to the stress involved. We then have:

At a fracture contact

$$\Delta G_s(contact) = \beta v_s(\sigma_c^{n\,2} + \sigma_c^{t\,2}) \quad (11)$$

On an aperture surface:

$$\Delta G_s(\theta) = \beta v_s[\sigma_p^n(\theta)^2 + \sigma_p^t(\theta)^2] \quad (12)$$

where $\Delta G_s(\cdot)$ is the strain energy at a specific location; v_s is the molar volume of the mineral of concern; and β is a proportionality constant.

Chemical potential and stress-activated mineral dissolution

The chemical potential at a specific point of a fracture surface depends on the local stress at that location. At a fracture contact, the chemical potential of the solid can be expressed as:

$$\mu_s = \mu_s^0 + \frac{1}{2}(\sigma_c^n + \sigma_c^t)v_s + \Delta G_s(contact) \quad (13)$$

where μ_s is the chemical potential of the mineral; μ_s^0 is the chemical potential at a standard (stress-free) state; *R* is the gas constant; and *T* is the absolute temperature. The second term on the right-hand side of Equation (13) represents the work done by the stress due to a volumetric expansion of a mineral grain as the mineral grows (Guéguen and Palciauskas, 1994). It is assumed that a thin water film exists at a fracture contact and this film is able to sustain the normal stress across the contact (e.g., Renard and Ortoleva, 1997). Similarly, at the aperture surface, the chemical potential of the solid at a specific point can be described by:

$$\mu_s(\theta) = \mu_s^0 + \frac{1}{2}[\sigma_p^n(\theta) + \sigma_p^t(\theta)]v_s + \Delta G_s(\theta) \quad (14)$$

The chemical potential of the dissolved species in the pore fluid can be written as:

$$\mu_a = \mu_a^0 + RTlnc_p + p_f v_a \quad (15)$$

where μ_a^0 is the chemical potential of dissolved species at the standard state; and v_a is the molar volume of the dissolved species.

The chemical affinity (A_p) for mineral dissolution at an aperture surface is calculated by:

$$A_p = \mu_s(\theta) - \mu_a = \mu_s^0 + \left\{\frac{1}{2}\left[\sigma_p^n(\theta) + \sigma_p^t(\theta)\right] + \beta\left[\sigma_p^n(\theta)^2 + \sigma_p^t(\theta)^2\right]\right\}v_s - \mu_a^0 - p_f v_a - RTlnc_p \quad (16)$$

Based on the transition state theory, the dissolution rate at an aperture surface can be described by (de Groot and Mazur, 1984; Dibble and Tiller, 1981; Dove, 1995):

$$R(\theta) = ke^{-\frac{\Delta G^{\#} + \sigma_p^t(\theta)v^{\#}}{RT}}\left(1 - e^{-\frac{A_p}{RT}}\right)$$

$$= ke^{-\frac{\Delta G^{\#}+\sigma_p^t(\theta)v^{\#}}{RT}}\left[1-\frac{C_p}{K(\theta)}\right] \quad (17)$$

where k is the reaction rate constant; $\Delta G^{\#}$ is the activation energy to account for the temperature effect on the reaction rate; $v^{\#}$ is the activation volume to account for the effect of surface stress on the reaction rate (Aziz et al., 1991; Yu and Suo, 2000); and $K(\theta)$ is the equilibrium constant of the dissolution reaction under stress:

$$K(\theta) = e^{\frac{\mu_s^0-\mu_a^0+\left\{\frac{1}{2}\left[\sigma_p^n(\theta)+\sigma_p^t(\theta)\right]+\beta\left[\sigma_p^n(\theta)^2+\sigma_p^t(\theta)^2\right]\right\}v_s-p_f v_a}{RT}} \quad (18)$$

Note that the concept of stress-activated mineral dissolution is an important component of the proposed model. This concept is based on the experimental observation that a tensile tangential stress at a solid surface enhances both mineral dissolution and growth at the surface (Aziz et al., 1991; Barvosa-Carter and Aziz, 1998; Yu and Suo, 2000). The activation volume $v^{\#}$ is estimated to be ~ 0.3 v_s (Aziz et al., 1991).

Reaction-diffusion at a fracture contact

The mass transfer between a fracture contact and the fluid in the surrounding aperture channel is facilitated by diffusion through a water film at the contact driven by a concentration gradient across the contact. Since the water film is usually very thin, on the order of nanometers (Alcantar et al., 2003), the water in the film is expected to quickly reach equilibrium with the confining solid. From Equation (13), the concentration of dissolved species at the fracture contact can then be estimated to be:

$$c_c = e^{\frac{\mu_s^0-\mu_a^0+\frac{1}{2}(\sigma_c^n+\sigma_c^t)v_s-p_f v_a+\Delta G_S(contact)}{RT}}. \quad (19)$$

Chemical species in nanopore confinement generally behave differently from those in a bulk system (Wang, 2014), which creates a difficulty with defining a standard state for a confined solute or solvent. To avoid this difficulty, we choose the pore fluid as a reference case for calculating the dissolved species concentration at the contact. In this sense, the calculated concentration should be treated as a nominal concentration, which is sufficient for our purpose since the main concern here is the concentration gradient across a fracture contact.

With Equation (19), the mineral dissolution rate at a fracture contact can be written as:

$$R(contact) = \frac{De^{-\frac{\Delta G_D^{\#}}{RT}}w(c_c-c_p)}{2g^2} \quad (20)$$

where w is the thickness of the water film at the contact and D is the diffusion coefficient of the dissolved species in water. The thickness of the water film depends on the confining stress across the fracture plane, the surface properties of minerals (e.g., surface charge density) and the

chemistry of the fluid. For simplicity, the following functional relationship is adopted to capture the effect of the confining stress on the water film thickness (Renard and Ortoleva, 1997):

$$w = \lambda\left(\sigma_c^n - p_f\right)^{-\gamma} \tag{21}$$

where λ and γ are adjustable constants. The water film becomes thinner as the confining stress σ_c^n increases.

Kinematics of aperture channel evolution

To further simplify the calculation for aperture surface dissolution, it is assumed that the shape of an aperture channel remains to be a truncated ellipse during fracture evolution. In this way, we can focus ourselves on the stress concentration only at two specific locations on the channel surface $\theta = 0$ or $\pi/2$:

$$\sigma_p^t(0) = p_f + \frac{(3-m)\sigma_\infty - 2(1+m)p_f}{1-m} \tag{22}$$

$$\sigma_p^t\left(\frac{\pi}{2}\right) = p_f - \frac{(1+m)\sigma_\infty + 2(1-m)p_f}{1+m}. \tag{23}$$

The geometry of a fracture aperture and a contact can then be determined by four independent variables: *a*, *b*, *h*, and g (Figs. 1 and 2). The evolution of fracture geometry is described by the following kinematic equations:

$$\frac{da}{dt} = v_s R(0) - \frac{da}{db} v_s R(contact) = -v_s R(0) - \frac{ha'^2}{ab'^2} v_s R(contact) \tag{24}$$

$$\frac{db}{dt} = -v_s R(contact) + v_s R\left(\frac{\pi}{2}\right) \tag{25}$$

$$\frac{dh}{dt} = -v_s R(contact) \tag{26}$$

$$l_0 = a + g = a_0 + g_0 \tag{27}$$

The last term in Equation (24) captures the effect of mineral dissolution at the fracture contact on the contact-area ratio of the fracture.

From a local scale to a global scale

Up to this point, the model is presented only in a local coordinate (*x'*, *y'*) (Fig. 2). To model fracture evolution on a whole fracture plane, this local description needs to be incorporated into global-scale mass continuity equations. In a global coordinate (*x*, *y*), variables *a*, *b*, *h*, and *e* not only evolve with time but also vary in space. The pore volume per unit fracture area can be defined as:

$$\phi = \frac{b(1-f_c)S}{4ab} \tag{28}$$

In an analogy to porous media (Oelkers, 1996), the tortuosity of aperture channels (τ) is assumed to be:

$$\tau = \frac{1}{1-f_c} \tag{29}$$

Assuming that the flow field in a truncated elliptic channel can be approximated by a normal elliptic channel with the same semi-axes, the permeability at each spatial point on a fracture plane can be calculated by (Lekner, 2007):

$$K = \frac{\pi(1-f_c)S(ab)^3}{16\eta b l_0(a^2+b^2)} \tag{30}$$

Similarly, the effective diffusion coefficient of the dissolved species can be calculated by:

$$D = \frac{(1-f_c)S}{4ab} D_0 \tag{31}$$

D_0 is the diffusion coefficient of the dissolved species in water. The mass continuity equations for the fluid and the dissolved species in the global coordinate can then be expressed by:

$$\frac{\partial \phi}{\partial t} = \vec{\nabla} \cdot (K \vec{\nabla} p_f) \tag{32}$$

$$\frac{\partial (\phi C_p)}{\partial t} = \vec{\nabla} \cdot \left(D \vec{\nabla} C_p + K C_p \vec{\nabla} p_f \right) + \frac{1}{2 l_0 v_s} \frac{\partial S}{\partial t} + 2R(contact). \tag{33}$$

2.3 RESULTS AND DISCUSSION

Shape evolution of a circular channel

The model formulated above has been tested against experimental observations on circular channels (Sprunt and Nur, 1977). In those experiments, a rectangular slab of a selected material with a centrically drilled hole was used (i.e., the cross section of the initial hole was circular). The slab was loaded uniaxially, producing non-uniform circumferential stress along the surface of the hole. The surface was kept in contact with a chemically reactive solution. The experiments showed that the dissolution on a free surface was to a large extent controlled by the tangential stress (i.e. the stress parallel to the surface), but not by the normal stress. Various shapes were induced by stress-mediated surface dissolution, including ellipses perpendicular to the uniaxial stress applied, ellipses parallel to the stress, flattened circles, and irregular shapes (Table 2). For a flattened circle, the radius of the hole increased as a function of θ from 90^o to ~ 60^o. Interestingly, the ellipses perpendicular to the stress seemed to occur in the solutions saturated with the material, while the ellipses parallel (and flattened circles) seemed to occur in undersaturated solutions.

From Equations (17) and (18), the shape evolution of an initially circular channel is determined by $r(\theta)$:

$$r(\theta) = \frac{R(\theta)e^{\frac{\Delta G^{\#}}{RT}}}{k} = e^{-\frac{\sigma_p^t(\theta)v^{\#}}{RT}}\left\{1 - \frac{\hat{c}_p}{e^{\frac{\left[0.5\sigma_p^t(\theta)+\beta\sigma_p^t(\theta)^2\right]v_S}{RT}}}\right\} \quad (34)$$

where $\hat{c}_p$ is the saturation degree of the pore fluid with respect to the mineral of concern under no stress conditions:

$$\hat{c}_p = c_p / e^{\frac{\mu_S^0 - \mu_a^0}{RT}}$$

The derivation of Equation (34) is based on the following considerations:

- For a circular channel, *m = 0* in Equation (10). Thus, $\sigma_p^t(0) = 3\sigma_\infty$ and $\sigma_p^t\left(\frac{\pi}{2}\right) = -\sigma_\infty$.
- $\sigma_p^n = p_f \ll \sigma_p^t(\theta)$. Thus, σ_p^n can be negligible in Equation (18).

The stress concentration around a circular channel surface is illustrated in Fig. 4A. As the eccentric angle θ increases from 0 to 90°, the tangential stress changes from a compressive to a tensile state. As shown in Equation (34), the relative dissolution rate at the channel surface depends on two factors. When the channel fluid is highly undersaturated, the dissolution rate depends only on the stress activation term $e^{-\frac{\sigma_p^t(\theta)v^{\#}}{RT}}$ in Equation (34), which increases with θ, such that $r\left(\frac{\pi}{2}\right)$ is always greater than $r(0)$, leading to the development of an elliptic channel parallel to the uniaxial stress applied (Fig. 4A). In contrast, as the saturation degree increases, the term $1 - \frac{\hat{c}_p}{e^{\frac{\left[0.5\sigma_p^t(\theta)+\beta\sigma_p^t(\theta)^2\right]v_S}{RT}}}$ in Equation (34) would take over the stress activation term, resulting in $r\left(\frac{\pi}{2}\right) < r(0)$ and therefore an ellipse perpendicular to the uniaxial stress (Fig. 4B). For a situation in between, the two competing factors interplay with each other, leading to a maximum dissolution rate at θ between 60 and 90°. In this case, a flattened circular channel would be developed. Therefore, the model proposed here is able to predict key experimental observations on the dissolution of an initially circular channel (Table 2). The model is also able to explain two other observations: the development of irregular hole shapes and the formation of dissolution striations on the limestone slab surface parallel to the uniaxial stress applied (Sprunt and Nur, 1977). It is known that, due to the stress-activation mechanism, a dissolving solid surface under a tensile tangential stress may become morphologically unstable (Aziz et al., 1991; Yu and Suo, 2000). This morphological instability may be responsible for the development of the observed irregular hole shapes and dissolution striations in the experiment.

This analysis, together with experimental observations (Sprunt and Nur, 1977), demonstrates the importance of a tangential stress in controlling mineral dissolution on a fracture channel surface. This mechanism has not been considered in any existing models. This raises an important issue with the current assumption of so-called "free surface dissolution". The existing models assume that mineral dissolution on the surface of a cavity embedded in a stressed rock depends only on the normal stress exerted by a hydrostatic pore fluid pressure (e.g., Liu et al.,

2006). This assumption is apparently inconsistent with the experimental observations discussed above.

In-situ determination of stress acting on a hydrocarbon reservoir is important for petroleum operations (Nawrocki et al., 1998; Haghi et al., 2013). The concept developed above may help develop a new stress indicator for estimating in-situ stress in an oil reservoir. Assume that a borehole is drilled into a limestone reservoir and an acid solution is injected into the borehole for enhanced oil recovery. Equation (34) indicates that by monitoring the shape evolution of an initially circular borehole due to mineral dissolution may allow us to estimate the magnitude and orientation of in-situ stress in a reservoir.

Criteria for channel opening and closure:

The aperture of a fracture channel is represented by the minor semi-axis of the truncated ellipse (2*b*). From Equation (25), the criteria for fracture opening or closure can be formulated as:

$$\omega = R\left(\frac{\pi}{2}\right)/R(contact)\begin{cases} > 1 & \text{fracture opening} \\ < 1 & \text{fracture closure} \end{cases} \tag{35}$$

Considering $p_f \ll \sigma_\infty$ and ignoring the term for strain energy, we have:

$$\omega \approx \frac{2g^2 k\sigma_\infty^\gamma}{\lambda K_{eq} D f_c^\gamma} \cdot \frac{(1-\hat{c}_p e^{\frac{\sigma_\infty v_S}{2RT}})}{(1-\hat{c}_p e^{-\frac{\sigma_\infty v_S}{2f_c RT}})} \cdot e^{-\frac{\Delta G^{\ddagger} - \Delta G_D^{\ddagger} + \sigma_\infty (0.5 v_S/f_C - v^{\ddagger}) - \Delta H_r}{RT}} \tag{36}$$

where ΔH_r is the enthalpy change for mineral dissolution; and K_{eq} is the solubility of the mineral under no stress. The second term on the right side is always less than unity, and so is the third term since $v^{\ddagger} < 0.3 v_s$ (Aziz et al., 1991) and $\Delta G^{\ddagger} > \Delta G_D^{\ddagger} + \Delta H_r$ for common rock-forming minerals such as quartz and calcite (see the data in Buxton et al., 1988; Drever, 1982; Wolery, 1994; Pokrovsky et al., 2009). Thus, a necessary condition for fracture opening is:

$$\frac{2g^2 k\sigma_\infty^\gamma}{\lambda K_{eq} D f_c^\gamma} > 1 \tag{37}$$

Thus the favorable conditions for fracture opening would include: a low solubility of the mineral (K_{eq}), a high reaction rate constant (k), and large contact areas (g). Since the second term on the right side of Equation (36) increases with reducing solution saturation with respect to the mineral, as expected, a dilute solution with a high flow rate would enhance fracture opening. Similarly, since the third term of the right side of the equation increases with temperature, an elevated temperature would also enhance fracture opening, as demonstrated in laboratory experiments (Yasuhara et a., 2006). The effect of confining stress (σ_∞) is more complicated: this stress may on one hand promote mineral solution at a fracture contact [the third term on the right side of Equation (36)] but on other hand may limit solute transport from the contact to the surrounding fracture channels by reducing the thickness of water film at the contact [the first term on the right side of Equation (36)]. Since the first effect is an exponential function of σ_∞, it is expected that a high σ_∞ would generally favor fracture closure (McGuire et al., 2013).

However, there may be a possibility that, under certain circumstances (e.g., large fracture contact areas, very thin water films at the contacts and a low saturation degree of incoming water), the pressure solution at the contact areas may be negligible compared to aperture surface dissolution. In this case, exerting a normal stress on a fracture plane may enhance fracture opening, as indicated by Equation (34), due to the activation effect of tangential surface stress on mineral dissolution. Such a situation may occur in an acid injection in a carbonate reservoir for enhanced oil recovery.

In an actual subsurface system, the incoming water, if not initially saturated, would rapidly become saturated as it percolates through a fracture, leading to fracture closure as indicated by the second term on the right side of Equation (36). In this sense, natural fractures tend to close. The situation could be different for an engineered subsurface system. For example, in an acid stimulation, the injected fluid can be maintained highly reactive by continuous fluid circulation. The most sensitive parameter for control in this case would be the reactive rate constant *k*, which can vary over orders of magnitude depending on the chemistry of the injected fluid. For example, in a carbonate rock, a high reaction rate can be induced by lowering the pH of the injected fluid, as demonstrated in laboratory experiments (McGuire et al., 2013).

Infiltration instability

Fracture opening usually involves preferential channeling (Elkhoury et al., 2013), which can be induced by reactive infiltration instability (Szymczak and Ladd, 2012). Because of this instability, certain modes of fluctuations (or perturbations) in fracture aperture can be amplified, leading to the fingering of a dissolution front. The actual spacing of the fingers (L_p) is determined by the perturbation with the maximum growth rate (Figure 5). Combined the model formulation presented above with a linear stability analysis provided by Szymczak and Ladd (2012), we obtain:

$$L_p \propto \frac{b^3}{k} e^{\frac{\Delta G^{\ddagger} - \sigma_{\infty} v^{\ddagger}}{RT}} \tag{38}$$

Equation (38) shows that, as the fracture aperture (b) reduces due to pressure solution, the spacing of the fingers decreases. Once the wave length of fingering falls within the experimental observation range, a spontaneous initiation of preferential channeling can then be observed (Fig. 5). This mechanism may be responsible for the observed spontaneous transition from a permeability reduction to a permeability increase in a static limestone experiment (Polak et al., 2004).

Model limitations and validation

The model presented above does not account for any impact of mechanical deformation of wall rocks on fracture closure, and its applicability may thus be limited to hard rocks such as carbonate rocks, sandstone, and igneous rocks. The model also does not consider the potential effect of secondary mineral precipitation within fractures, which may alter the hydrologic properties of the fracture. Furthermore, the model does not consider a possible effect of a shear stress acting on a fracture plane. It is known that a shear displacement can cause fracture aperture

dilation (Min et al., 2004; Nemoto et al., 2009). These processes need to be considered in a future improvement to the model.

As shown above, the model developed is able to provide a reasonable explanation for key features of fracture evolution in laboratory experiments, including a spontaneous transition from a permeability reduction to a permeability increase (Polak et al., 2004), a potential enhancement of fracture opening by temperature (Yasuhara et a., 2006), and fracture opening by a low-pH solution (McGuire et al., 2013). The model also provides a reasonable prediction for the shape evolution of initially circular holes in stressed geomaterials (Sprunt and Nur, 1977). These qualitative comparisons can be viewed as a first-order validation for the model. More quantitative validations will be needed. Further validations can be performed against data sets collected from various column experiments (e.g., Yasuhara et al., 2006; Polak et al., 2004; McGuire et al., 2013; Ellis et al., 2013; Elkhoury et al., 2013) by directly solving continuity equations (32-33) for the experimental systems. Note that the model presented here focuses only on a single fracture. Once validated, this model can be incorporated into a reservoir simulator for large-scale simulations. The model will provide the needed information about fracture permeability evolution for reservoir-scale simulations.

2.4 CONCLUSIONS

A dynamic model for subsurface fracture opening and closure has been formulated. The model explicitly accounts for the stress concentration around individual aperture channels and the stress-activated mineral dissolution. It has been demonstrated that the surface stress-activated dissolution may play an important role in subsurface fracture evolution. Based on a model analysis, a necessary condition for fracture opening has been derived. The proposed model is able to explain key features of fracture evolution in laboratory experiments. The geologic implications of the model results have been discussed. The work presented here may help to develop a new method for estimating in-situ stress in a reservoir.

2.5 REFERENCES

Alcantar, N., Isrealachvili, J., Boles, J., 2003. Forces and ionic transport between mica surfaces: implications for pressure solution. Geochim. Cosmochim. Acta 67, 1289–1304.

Aziz, M. J., Sabin, P. C., Lu. G.-Q., 1991. The activation strain tensor: Nonhydrostatic stress effects on crystal-growth kinetics. Phys. Rev. B, 44, 9812-9816.

Barvosa-Carter, W. Aziz, M. J., 1998. Kinetically driven growth instability in stressed solids. Phys. Rev. Letters, 81, 1445-1448.

Beeler, N. M., Hickman, S. H., 2004. Stress-induced, time-dependent fracture closure at hydrothermal conditions. J. Geophys. Res., 109, B02211.

Bruton, C. J., Helgeson, H. C., 1983. Calculation of the chemical and thermodynamic consequences of differences between fluid and geostatic pressure in hydrothermal systems. Am. J. Sci., 283-A, 540-588.

Buxton, G. V., Greenstock, C. L., Helman, W. P., Ross, A. B., 1988. Critical review of rate constants for reactions of hydrated electrons, hydrogen atoms and hydroxyl radicals (·OH-/·O-) in aqueous solution. J. Phys. Chem. Ref. Data, 17, 513-886.

Chuang, T.-J., Fuller, Jr., E., 1992. Extended Charles-Hilling Theory for stress corrosion cracking of glass. J. Am. Ceram. Soc., 75, 540-545.

De Groot, S. R., Mazur P., 1984. Non-Equilibrium Thermodynamics, North-Holland Pub. Co., Amsterdam.

Dibble, W. E., Tiller, W. A., 1981. Non-equilibrium water/rock interactions – I. Model for interface-controlled reactions. Geochim. Cosmochim. Acta, 45, 79-92.

Dove, P. M., 1995. Geochemical controls on the kinetics of quartz fracture at subcritical tensile stresses. J. Geophys. Res., 100, 22349-22359.

Drever, J. I., 1982. The Geochemistry of Natural Waters. Prentice-Hall, Englewood Cliffs, NJ.

Elkhoury, J. E., Ameli, P., Detwiler, R. L., 2013. Dissolution and deformation in fractured carbonates caused by flow of CO_2-rich brine under reservoir conditions. Inter. J. Greenhouse Gas Control, 16S, S203-S212.

Ellis, B. R., Fitts, J. P., Bromhal, G. S., McIntyre, D. L., Rappero, R., Peters, C. A., 2013. Dissolution-driven permeability reduction of fractured carbonate caprock. Environ. Eng. Sci., 30, 187-193.

Ghassemi, A., Kumar, G. S., 2007. Changes in fracture aperture and fluid pressure due to thermal stress and silica dissolution/precipitation induced by heat extraction from subsurface rocks. Geothermics, 36, 115-140.

Guéguen, Y., Palciauskas, V., 1994. Introduction to the Physics of Rocks. Princeton University Press, Princeton, N.J.

Haghi, A. H., Kharrat, R., Asef, M. R., 2013. A case study for HCL-based fracturing and stress determination: A Deformation/Diffusion/Thermal approach. J. Petroleum Sci. Eng., 112, 105-116.

Lekner, J., 2007. Viscous flow through pipes of various cross-sections. Eur. J. Phys., 28, 521-527.

Liu, H.-H., Wei, M.-Y., Rutqvist, J., 2013. Normal-stress dependence of fracture hydraulic properties including two-phase flow properties. Hydrogeology J., 21, 371-382.

Liu, J., Polak, A., Elsworth, D., Grader, A., 2005. Dissolution-induced preferential flow in a limestone fracture. J. Contaminant Hydrology, 78, 53-70.

Liu, J., Sheng, J., Polak, A., Elsworth, D., Yasuhara, H., Grader, A., 2006. A fully-coupled hydrological-mechanical-chemical model for fracture sealing and preferential opening. Inter. J. Rock Mech. Ming Sci., 43, 23-36.

McGuire, T. P., Elsworth, D., Karcz, Z., 2013. Experimental measurements of stress and chemical controls on the evolution of fracture permeability. Transp. Porous Med., 98, 15-34.

Memoto, K., Watanabe, N., Hirano, N., Tsuchiya, N., 2009. Direct measurement of contact area and stress dependence of anisotropic flow through rock fracture with heterogeneous aperture distribution. Earth Planet. Sci. Lett., 281, 81-87.

Min, K.-B., Rutqvist, J., Tsang, C.-F., Jing, L., 2004. Stress-dependent permeability of fractured rock masses: a numerical study. Inter. J. Rock Mech. Mining Sci., 41, 1191-1210.

Nawrocki, P. A., Dusseault, M. B., Bratli, R. K., 1998. Use of uniaxial compression test results in stress modeling around openings in nonlinear geomaterials. J. Petroleum Sci. Eng., 21, 79-94.

Neretnieks, I., 2014. Stress-mediated closing fractures: Impact of matrix diffusion. J. Geophys. Res. Solid Earth, 119, 4149-4163.

Oelkers, E. H., 1996. Physical and chemical properties of rocks and fluids for chemical mass transport calculations. Review in Mineralogy, 34, 131-191.

Pokrovsky, O. S., Golubev, S. V., Schoot, J., Castillo, A., 2009. Calcite, dolomite and magnesite dissolution kinetics in aqueous solutions at acid to circumneutral pH, 25 to 150°C and 1

to 55 atm CO_2: New constraints on CO_2 sequestration in sedimentary basins, Chemical Geology, 265, 20-32.

Polak, A., Elsworth, D., Liu, J., Grader, A. S., 2004. Spontaneous switching of permeability changes in a limestone fracture with net dissolution. Water Resources Res., 40, W03502.

Pyrak-Nolte, L. J., Morris, J. P., 2000. Single fractures under normal stress: The relation between fracture specific stiffness and fluid flow. Inter. J. Rock Mech. Mining Sci., 37, 245-262.

Renard, F., Ortoleva, P., 1997. Water films at grain-grain contacts: Debye-Hückel, osmotic model of stress, salinity, and mineralogy dependence. Geochim. Cosmochim. Acta, 61, 1963-1970.

Reuschlé, T., Trotignon, L., Gueguen, Y., 1988. Pore shape evolution by solution transfer: thermodynamics and mechanics. Geophys. J., 95, 535-547.

Shimizu, I., 1995. Kinetics of pressure solution creep in quartz: theoretical consideration. Tectonophysics, 245, 121-134.

Souley, M., Lopez, P., Boulon, M., Thoraval, A., 2015. Experimental hydromechanical characterization and numerical modeling of a fractured and porous sandstone. Rock. Mech. Rock Eng., 48, 1143-1161.

Sprunt, E. S., Nur, A., 1977. Experimental study of the effects of stress on solution rate. J. Geophys. Res., 82, 3013-3022.

Szymczak, P., Ladd, A. J. C., 2009. Wormhole formation in dissolving fractures. J. Geophys. Res., 114, B06203.

Szymczak, P., Ladd, A. J. C., 2012. Reactive-infiltration instabilities in rocks. Fracture dissolution. J. Fluid Mech., 702, 239-264.

Wang, Y., 2014. Nanogeochemistry: Nanostructures, emergent properties and their control on geochemical reactions and mass transfers. Chemical Geology, 378-379, 1-23.

Wang, G.-J., Vitek, V., 1986. Relationships between grain boundary structure and energy. Acta Metall., 34, 951-960.

Wolery, W. G., 1994. Dissolution Kinetics and Mechanisms in Quartz-and Granite-Water Systems. Ph.D. Dissertation, Massachusetts Institute of Technology.

Xie, L. Z., Gao, C., Ren, L., Li, C. B., 2015. Numerical investigation of geometrical and hydraulic properties in a single rock fracture during shear displacement with Novier-Stokes equations. Environ. Earth Sci., 73, 7061-7074.

Yasuhara, H., Elsworth, D., 2004. Evolution permeability in a natural fracture: Significant role of pressure solution. J. Geophys. Res., 109, B03204.

Yasuhara, H., Elsworth, D., 2006. A numerical model simulating reactive transport and evolution of fracture permeability. Inter. J. Numer. Anal. Meth. Geomech., 30, 1039-1062.

Yasuhara, H., Elsworth, D., 2008. Compaction of a rock fracture moderated by competing roles of stress corrosion and pressure solution. Pure Appl. Geophys., 165, 1289-1306.

Yasuhara, H., Polak, A., Mitani, Y., Grader, A. S., Halleck, P. M.,, Elsworth, D., 2006. Evolution of fracture permeability through fluid-rock reaction under hydrothermal conditions. Erath Planet Sci. Letters, 244, 186-200.

Yasuhara, H., Kinoshita, N., Ohfuji, H., Lee, D. S., Nakashima, S., Kishida, K., 2011. Temporal alteration of fracture permeability in granite under hydrothermal conditions and its interpretation by coupled chemo-mechanical model. Appl. Geochem., 26, 2074-2088.

Yu, H. H., Suo, Z., 2000. Stress-dependent surface reactions and implications for a stress measurement technique. J. Appl. Phys., 87, 1211-1218.

Zhao, Z., Liu, L., Neretnieks, I., Jing, L., 2014. Solute transport in a single fracture with time-dependent aperture due to chemically mediated changes. Inter. J. Rock Mechanics Mining Sci., 66, 69-75.

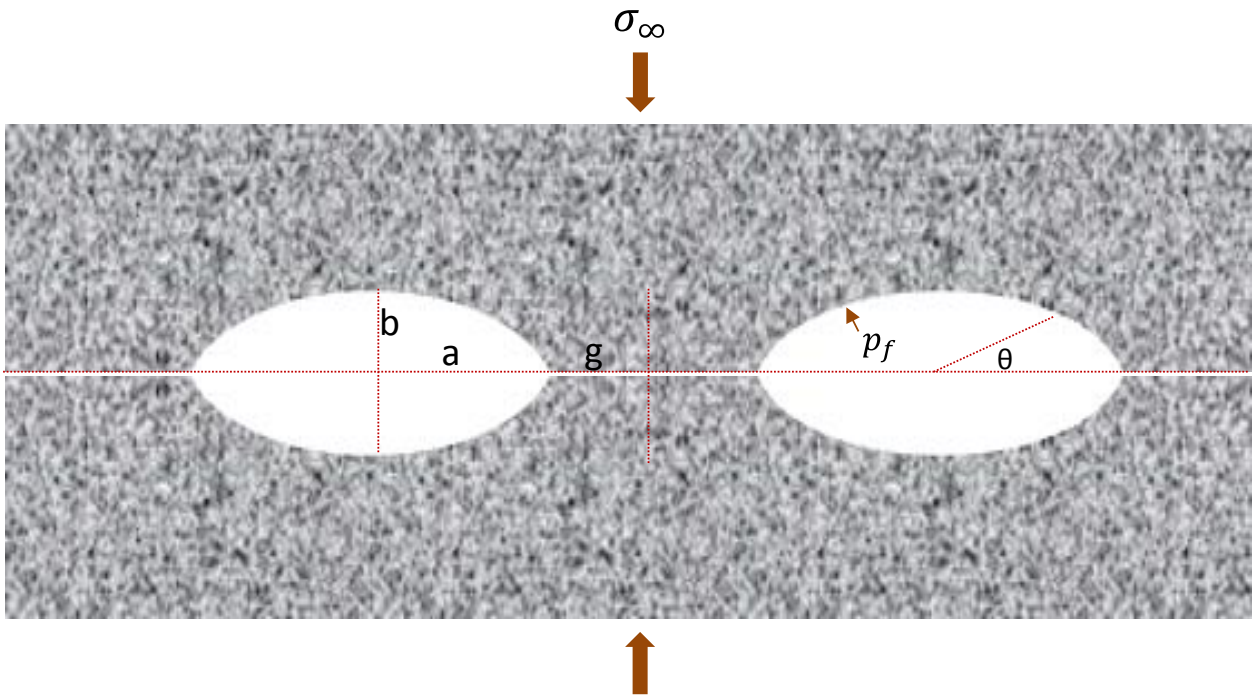

Figure 1: Representation of a single fracture plane with truncated elliptic channels surrounding fracture contact areas

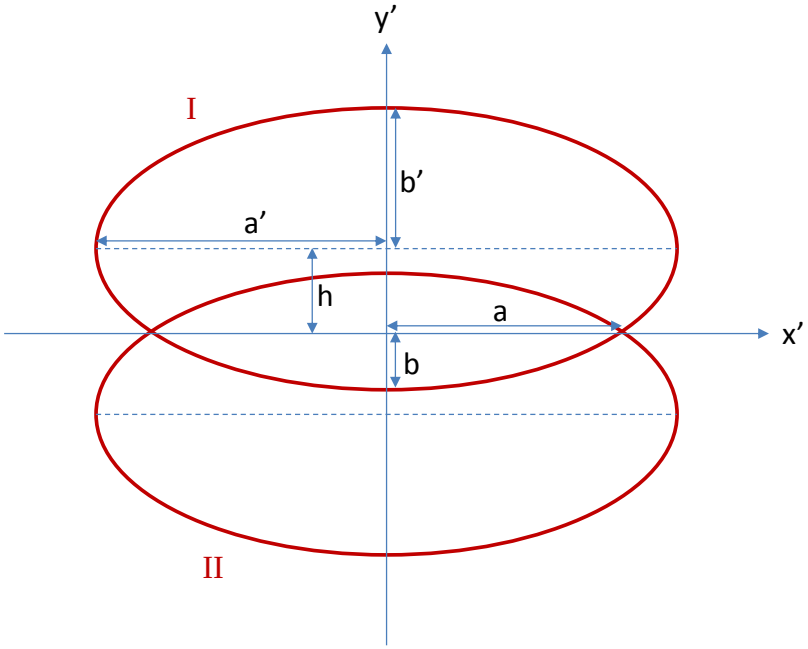

Figure 2: Geometric representation of a truncated elliptic channel

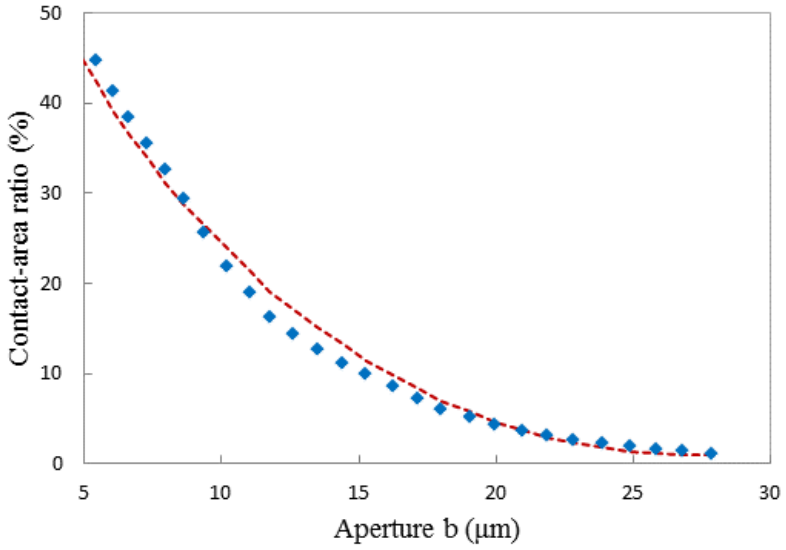

Figure 3: Model fitting to the measured aperture-contact area relation. Data are taken from Yasuhara et al. (2006).

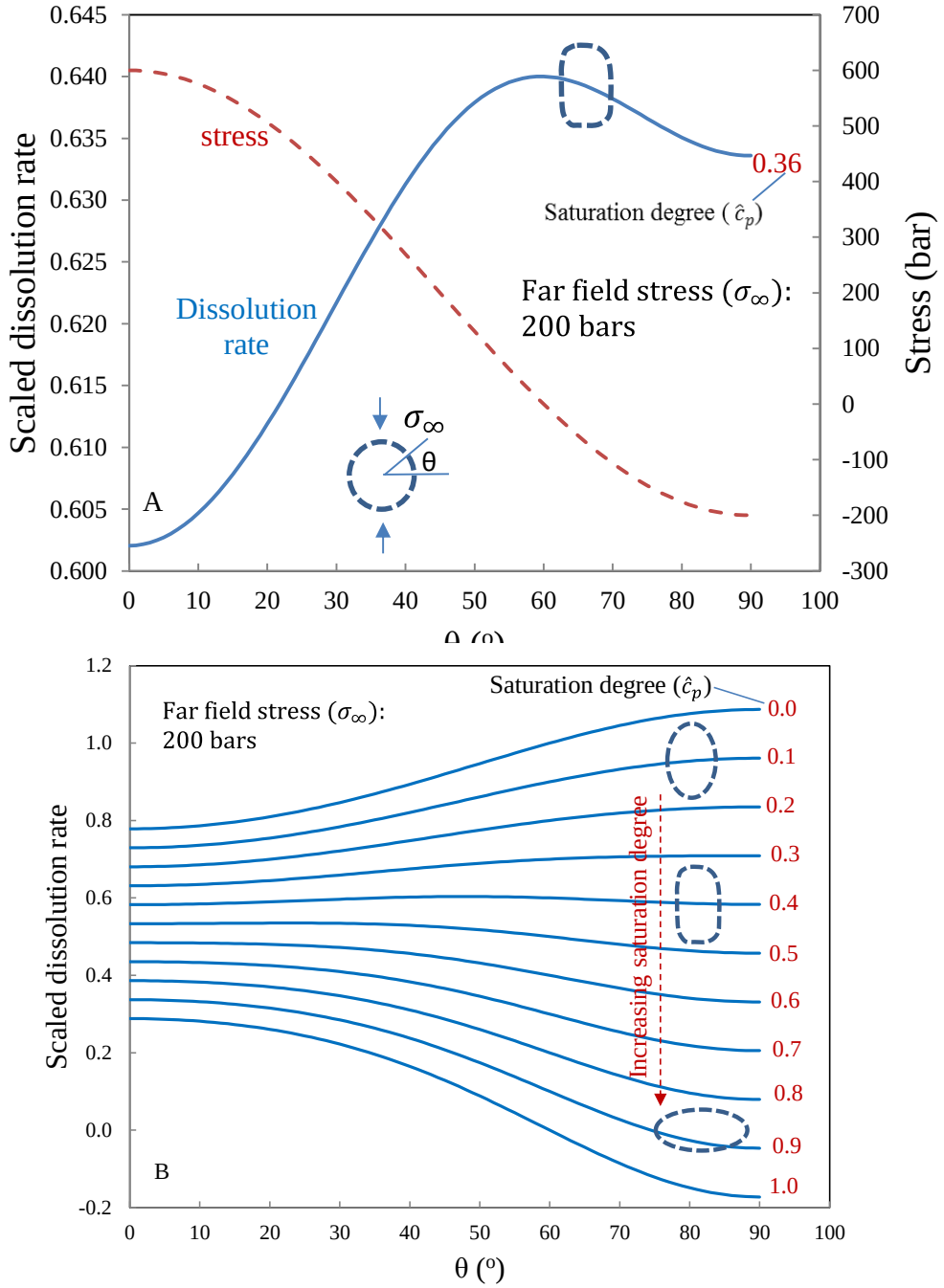

Figure 4: A) Stress distribution around a circular channel and dissolution rate that leads to the development of a flattened circle; B) evolution of an initially circular hole under stress as controlled by the saturation degree of pore fluid. v_s= 36.9 cm^3/mol; R = 83.1 cm^{3}bar/mol/K; T = 25 ^{o}C; β = 2.86x10^{-6} bar^{-1}.

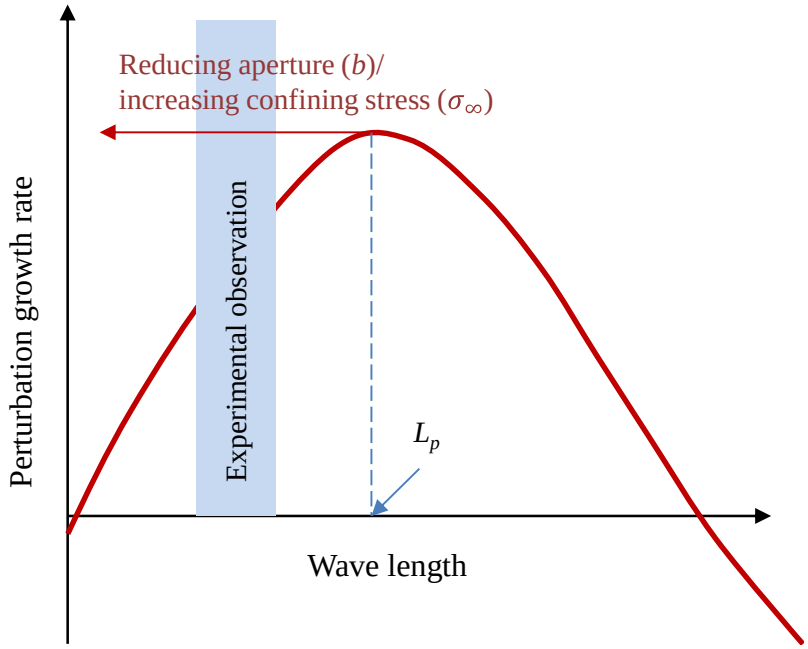

Figure 5: Spontaneous initiation of aperture channeling. As the fracture aperture reduces due to pressure dissolution, the preferred wave length of dissolution fingering decreases. Once the preferred wave length falls within the experimental observation range, a spontaneous initiation of preferential channeling can be observed.

Table 1. Survey of models for fracture opening and closure. H – hydrologic model; M – mechanical model; HC- hydrologic-chemical model; HM – hydrologic-chemical model; MC – mechanical-chemical model; HMC - hydrologic-mechanical-chemical model; THMC – thermal-hydrologic-mechanical-chemical model.

Type	Model	Processes considered	Note
H	Xie et al. (2015)	Aperture variations due to shear displacement; Navier-Stokes flow in fracture	Purely geometrical for aperture calculations; no mechanics and chemistry considered.
M	Liu et al. (2013)	Two-part Hooke's deformation of fracture aperture	Providing an interesting connection between fracture hydrologic properties (e.g., capillary pressure and relative permeability) and the confining normal stress.
HC	Liu et al. (2005)	Dissolution-induced preferential flow; Advective flow in fracture (cubic law);	No mechanical processes considered.
	Szymczak & Ladd (2009; 2012)	Mineral dissolution; Advective flow in fracture (cubic law); Reactive-infiltration in stability	Detailed analysis on reactive-infiltration instability in a fracture; no consideration of mechanical processes.
HM	Zhao et. (2014)	Pressure solution at contacting asperities; Advective flow in fracture (cubic law); Matrix diffusion in porous fracture walls; Empirical contact area ratio vs. aperture	No consideration of fluid chemistry and mineral dissolution on fracture aperture surface.
	Souley et al. (2015)	Linear elasticity in rock matrix; Nonlinear normal behavior of fracture; Elastic and perfectly plastic behavior of fracture in shear direction; Advective flow in fracture (cubic law)	Purely mechanical and hydrological; no chemistry considered.
	Nemoto et al. (2009)	Experimentally determined aperture distribution; Advective flow in fracture (cubic law)	Emergence of directional heterogeneity in fracture aperture due to a shear displacement.
	Min et al. (2004)	Nonlinear normal deformation (empirical); Shear dilation of fracture (empirical); Advective flow in fracture (cubic law)	Focus on discrete fracture networks; no chemical process considered.
	Pyrak-Nolte & Morris (2000)	Fracture stiffness; Fracture aperture deformation; Fluid flow in fracture	Providing a possible connection of fracture flow to fracture aperture and contacting area through fracture stiffness, which can be measured in a field through a geophysical method.
	Beeler & Hickman	Pressure solution of prop;	Applicable only to fracture

MC	(2004)	Crack stiffness; Water saturation degree w/r prop material; Effect of curvature on prop solubility	closure induced by prop dissolutions.
HMC	Liu et al. (2006)	Pressure solution at contacting asperities; Free surface dissolution in fracture voids; Channel flow	Providing a geometrical relationship between aperture and asperity dissolution. Not able to explain a spontaneous switch from fracture closure to opening.
	Neretnieks (2014)	Pressure dissolution at contacting asperities Mineral dissolution/precipitation on fracture void surfaces; Matrix diffusion and mineral precipitation	Showing that matrix diffusion might be important for fracture closure.
THMC	Ghassemi & Kumar (2007)	Fracture aperture change due to thermoelasticity; Advective flow in fracture (cubic law); Heat transport in the fracture; Solute transport; Aperture change to due to mineral dissolution	No consideration of the effect of confining stress on fracture closure.
	Yasuhara & Elsworth (2004; 2006; 2008); Yasuhara et al. (2011)	Temperature-dependent mineral dissolution and chemical diffusion; Pressure solution at contacting asperities; Stress corrosion at contacting asperities; Free surface dissolution in fracture voids; Empirical contact area ratio vs. aperture; Advective flow in fracture (cubic law)	No consideration of the possible effect of surface stress on mineral dissolution on fracture void surface.

Table 2: Resulting shape of an initially circular hole due to stress-mediated dissolution (Sprunt and Nur, 1977)

Material & solution	Axial load (bars)	Hole shape
In salt solution		
Salt undersaturated 1	30	Flattened circle
Salt undersaturated 2	12	Flattened circle
Salt undersaturated 3	13	Flattened circle
Salt saturated 1	15	Ellipse perpendicular
Salt saturated 2	14	Ellipse perpendicular
	In dilute hydrochloric acid	
Solenhofen limestone 3	129	Ellipse parallel
Solenhofen limestone 4	66	Ellipse parallel
Solenhofen limestone 6	45	Ellipse perpendicular
Oak Hall limestone 1	297	Ellipse perpendicular
Oak Hall limestone 3	324	Ellipse perpendicular
Oak Hall limestone 4	170	Ellipse perpendicular
Oak Hall limestone 5	262	Ellipse perpendicular
Kasota limestone	59	Ellipse perpendicular
Marble 1	220	Flattened circle
Marble 2	187	Flattened circle
Marble 3	91	Flattened circle
Water lime 1	48	Irregular
Water lime 1	42	Irregular
Water lime 1	29	Irregular
Chalk 1, Kansas	39	Irregular
Chalk 2, Kansas	24	Irregular

3. DECOVALEX 2015 - TASK C2: MODELING OF FLOW AND TRANSPORT AT BEDRICHOV SITE

3.1 INTRODUCTION

Flow and transport in fracture networks remains one of the more challenging issues facing hydrogeologists today. Accurate predictions of ow and transport in fracture networks is important in a variety of hydrogeological problems including: nuclear waste repository safety assessment, contaminant transport and remediation, unconventional hydrocarbon production, enhanced geothermal energy production and mine reclamation. Fractured reservoirs are characterized by extreme heterogeneity and data scarcity. Generally, it is not possible to uniquely determine the spatial distribution of fracture network properties and provide a complete description of the system behavior; however, simple models which incorporate field data at the appropriate scale, should be able to provide insight into the salient feature of the system behavior (Neuman, 2005). The transport time distribution is a powerful description of the ow and transport in a hydrogeologic system; however, little is known about the field scale transit time distribution in fracture networks. Lumped parameter models provide a simplified methodology to investigate the residence time distribution in fracture networks.

Transport in fracture networks is affected by rapid advection in fractures and diffusion into and out of adjacent intact lower-permeability matrix (e.g. Haggerty et al., 2001); Maloszewski and Zuber, 1990, 1985; Neretnieks, 1980; Sudicky and Frind, 1982; Tang et al., 1981). The effect of matrix diffusion is to slow tracer transport compared to the advective fluid velocity, dampen concentration variation and produce long tailing of tracer release (Cook and Robinson, 2002; Maloszewski and Zuber, 1985; Neretnieks, 1980, 1981). Tracer transport in fractured networks has been evaluated theoretically and used to interpret tracer transport experiments with a variety of models from analytical models of simple geometry to numerical models of discrete fracture networks. Multiple continuum models allow linear exchange between the advective and immobile porosities for a single rate (Warren and Root, 1963) to multiple mass transfer rates (Haggerty and Gorelick, 1995). Analytical solutions exist for models that account for concentration gradients in the matrix for simple geometries such as a single fracture (Tang et al, 1981), parallel fractures (e.g. Maloszewski and Zuber, 1990, 1985; Sudicky and Frind, 1982)) and a distribution of different matrix block shapes and sizes (e.g. Haggerty et al., 2000). Discrete fracture network models have been used to develop fully distributed reactive ow and transport models (e.g. Therrien and Sudicky, 1996) as well as produce uid velocity fields for particle tracking schemes which can be post processed to account for matrix interactions (e.g. Painter and Cvetkovic, 2005; Painter et al., 2008; Roubinet et al., 2013). The parameters used in these models are a strong function of the spatial and temporal scale of interest (Neuman, 2005; Shapiro, 2001), thus observations used to estimate fracture parameters should be made at similar length and time scales to the desired predictions.

Environmental tracers can provide a rich dataset which can be used to understand fracture ow and transport over a wide range of spatial and temporal scales. Environmental tracer concentrations have been used to develop conceptual models of tracer transport, and constrain fracture network parameters in a variety of fractured rock systems. Cook and Robinson (2002) develop an analytical model of environmental tracer transport in parallel fractures and show that tracer concentrations could not uniquely determine fracture network properties, but were capable

of providing some constraint fracture spacing, aperture and recharge. Cook et al. (2005) use this model to constrain the recharge rate in a fractured, porous aquifer in South Australia, and show that this simple model was a reasonable representation of a more complex system and could be used prediction concentration breakthrough.

Groundwater mean age can be used to characterize the residence time distribution in fracture networks. Analytical models of mean groundwater age have been developed in fractured systems (Doyon and Molson, 2012). Groundwater age in the field is often determined using environmental tracer concentrations. However, in fracture networks, environmental tracer concentrations provide the solute residence time, which is not equal to the advective residence time (Neretnieks, 1981). Thus, "apparent" groundwater ages determined from environmental tracers will be older than the advective fluid residence time (Cook and Robinson, 2002), and the use groundwater age in fractured systems must incorporate matrix interactions.

The residence time distribution is a fundamental characteristic of a ow system and provides critical information for determining the parameters controlling flow and transport in the system. Residence time distributions have been developed for a variety of simplistic aquifers (Cook and Herczeg, 2000; Maloszewski and Zuber, 1996). These models provide a convenient method to investigate the residence time and ow path distribution in hydrogeologic systems (e.g. Gardner et al., 2010, 201); Solomon et al., 2010, 2015). Lumped Parameter models in conjunction with tracer transport observations provide a means to investigate the residence time distribution and infer ow path characteristics in a reservoir (Danckwerts, 1953). Multiple environmental tracers can be used to identify the best age distribution and mixing models which best fit the observed data (Gardner et al, 2011; Solomon et al., 2010). McCallum et al. (2014) show that age tracers have limited ability to uniquely identify the age distribution, but indicate the time series of tracers can help reduce uncertainty. Solomon et al (2010) indicate that the mean ages derived from multiple environmental tracers appears to be robust to choice the transit time distribution. However, these studies were carried out for porous ow aquifers and the application of lumped parameter models in fractured ow systems to estimate the transit time distribution is questionable.

The aim of this paper is to provide some insight into the uncertainty in estimating the mean transit time and the ability to distinguish the transit time distribution in fracture networks discharge to single fractures at the scale of 100's of meters using lumped parameter models and multiple environmental tracer concentrations. We utilize time series of $\delta^{18}O$, $\delta^{2}H$ and ^{3}H along with CFC measurements from individual fractures in the Bedrichov Tunnel of the Czech Republic to investigate the TTD in several fracture networks of varying length and discharge. We compare several transit time distributions, including a developed TTD which includes the effects matrix diffusion. We identify best fit mean ages for each TTD, and compare the ability of each TTD to fit the observed tracer concentrations and the effect of choosing different TTD on the mean age estimation.

3.2 THEORY

Lumped parameter models were developed to investigate residence time distributions in chemical reactors where the true distribution of ow paths is not known (Danckwerts, 1953). The breakthrough curve of a tracer transported through the reactor can be used to provide information

on the distribution of ow paths, and the processes affecting transport in the reactor, for example the amount of dead volume, the degree of mixing, and the amount of dispersion in 1-D ow in the reactor (Danckwerts, 1953). The residence time distribution has been used to investigate ow and transport in groundwater systems where the exact distribution of flow paths is unknown for many decades (e.g. Maloszewski and Zuber, 1996). The concentration at time t is given by the convolution integral:

$$C(t) = \int_0^\infty C_{in}(t-t')g(t')e^{-\lambda t}dt', \tag{1}$$

where t is the residence time, and λ is the decay constant of a radioactive tracer, $C_{in}(t)$ is the historical input at recharge and $g(t)$ is the residence time distribution for the flow paths discharging to the sampling point. Equation 1 along with observations of tracer concentration in groundwater allows for the investigation of the distribution of ow paths and the processes affecting transport in the "black box" ow system which feeds the discharge point.

Residence Time Distribution

The residence time distribution contains the ow and transport information for the system upstream of the sampling point and has been derived for several simplified aquifer types (Cook and Herczeg, 2000; Maloszewski and Zuber, 1996). Here we consider two existing transit time distributions which encompass two possible end members of reservoir types, and develop a distribution which incorporates matrix diffusion. The simplest age distribution considered is for water flowing along a single ow path or fracture subject to longitudinal dispersion, termed here as the dispersion distribution which can be written (Maloszewski and Zuber, 1982):

$$g(t') = t'^{-1}\left(4\pi P_e t'/\tau\right)^{-1/2} exp\left[\frac{-\tau*(1-t'/\tau)^2}{4P_e t'}\right], \tag{2}$$

where $Pe = D/vx$ is the system Peclet number with longitudinal dispersivity D, velocity v and transport distance x, and τ is the mean transit time.

An exponential distribution of residence times is achieved when there is complete mixing of an even distribution of ow paths of all ages, thus represents an end member where many different flow paths converge to the sampled fracture. The exponential distribution is written (Maloszewski and Zuber, 1982):

$$g(t') = \frac{1}{\tau}e^{-\frac{t'}{\tau}}. \tag{3}$$

Equations 2 and 3 were developed for porous media aquifers and do not consider the effect of diffusion into immobile regions on the transit time. In this study, a transit time distribution is developed that includes the effects infinite matrix diffusion for a constant fracture aperture. Here,

we assume that the diffusion time to equilibrate matrix blocks with the fracture fluid is long compared to the changes in concentration, and that the fracture system is uniform.

The total transport time distribution ($g_{tran}(t_{tran})$) can be written as the convolution of the advective travel time distribution g(t0) and the retention time distribution ($g_{ret}(t_{ret})$) coupled by a velocity dependent transport resistant parameter distribution (Painter et al, 2008):

$$g_{tran}(t_{tran}) = \int_0^{\infty} \int_0^{t_{tran}} g_{ret}(t_{tran} - t'|\beta) f_{\beta|t'}(\beta|t') g(t') dt' d\beta, \tag{4}$$

where $t_{tran} - t' = t_{ret} \geq 0$ is the retention time from matrix diffusion and β is the spatially variable velocity dependent transport resistance parameter with a density distribution of $f_{\beta/t'}(\beta/t')$. If variability in the resistance parameter is neglected (Painter et al, 2008):

$$f_{\beta|t'}(\beta|t') = \delta(\beta - t'\bar{\beta}/\tau) \tag{5}$$

where δ is the Dirac function. In fractured rock applications, the resistance parameter is defined (Painter et al, 2008):

$$\beta(t') = \int_0^{t'} \frac{ds}{b(s)}, \tag{6}$$

where b is the fracture half aperture and s is distance along the flow path. If a constant aperture is assumed then (Painter et al, 2008):

$$\beta = \frac{t'}{\bar{b}} = t' \frac{\bar{\beta}}{\tau}, \tag{7}$$

where $\bar{b}$ is the effective fracture aperture for the system of interest.

Painter et al (2008) present retention time distributions for a wide variety of subsurface transport processes. For this paper, unlimited matrix diffusion is considered. The retention time distribution for infinite matrix diffusion is:

$$g_{ret}(t_{ret}|\beta) = \frac{\kappa\beta}{2\sqrt{\pi} t_{ret}^{3/2}} exp\left[\frac{-\kappa^2\beta^2}{4t_{ret}}\right], \tag{8}$$

where $\kappa = \theta_{im}\sqrt{D_{im}}$ is a function of the matrix porosity θ_{im} and the matrix diffusion coefficient D_{im}.

The concentration at time *t* for a system which includes matrix diffusion can now be written:

$$C(t) = \int_0^\infty C_{in}(t - t_{tran}) g_{tran}(t_{tran}) dt_{tran}. \tag{9}$$

Inserting equation 4 into equation 9 and assuming constant aperture and no variance in the resistance transport parameter (equations 7 and 5) gives:

$$C(t) = \int_0^\infty C_{in}(t - t_{tran}) \int_0^{t_{tran}} g_{ret}(t_{tran} - t'|\beta)(t'/\bar{b}) g(t') dt' dt_{tran}. \tag{10}$$

Equation 10 describes the transit time distribution, and the resulting concentration expected in fracture discharge at time *t* and is a function of the purely advective travel time, modified by retention from diffusion into the adjacent matrix. Here, ow along a single constant aperture fracture is considered, thus the advective travel time is assumed to the dispersive distribution (equation 2). Equation 10 is then parameterized by the mean advective travel time τ, the longitudnal dispersivity Pe, the fracture aperture $\bar{b}$, matrix porosity θ_{im} and diffusivity D_{im}.

Seasonal Input Function

The concentration input history $C_{in}(t)$ in equations 1 and 10 is the historical concentration of a given tracer in water recharging the aquifer system. The concentration of these tracers is generally measured in precipitation and/or the atmosphere. The concentration in recharge will be modified from the atmospheric or precipitation concentration by the processes occurring during recharge such as soil flow, evapotranspiration and seasonality of precipitation. When recharge is constant throughout the year, C_{in} will be equal to the concentration in precipitation. However, in cases where the concentration of the tracer changes seasonally, seasonality in precipitation, infiltration or evapotranspiration can cause C_{in} to differ from the atmospheric or precipitation record. These effects are especially important for stable isotopes of water and tritium. The annual flux weighted average concentration of tracer ($C_{in_{an}}$) is given by:

$$C_{in_{an}} = \frac{\sum_{i=1}^{12} C_i \alpha_i P_i}{\sum_{i=1}^{12} \alpha_i P_i}, \tag{11}$$

where $\alpha_i = R_i/P_i$ the recharge fraction is fraction of precipitation which become recharge for the *i*th month. In the area of the Bedrichov Tunnel winter is wetter and colder with precipitation predominantly falling as snow, and is a time of low evapotranspiration potential. During the summer months, precipitation falls as rain and there is a high evapotranspiration potential, thus there is a significant potential for seasonality in the recharge function.

To investigate the effects of seasonality we split the year into two seasons - summer and winter - and assume constant recharge fractions for summer months (α_s) and winter months (α_w). If the seasonal infiltration ratio $\alpha = \alpha_s/\alpha_w$ is defined, the seasonal recharge can be approximated by (Zuber and Maloszewski, 2001):

$$C_{in_{an}} = \frac{(\alpha \sum_{i=4}^{9} C_i P_i)_s + (\sum_{i=10}^{3} C_i P_i)_w}{(\alpha \sum_{i=4}^{9} P_i)_s + (\sum_{i=10}^{3} P_i)_w}, \tag{12}$$

where the summer months are assumed to be April through October and winter months November through March. The mean stable isotope composition of groundwater can be used to estimate α:

$$\alpha = \frac{(\sum_{i=3}^{10} P_i \delta_i)_w - \delta(\sum_{i=3}^{10} P_i)_w}{\delta(\sum_{i=4}^{9} P_i)_s - (\sum_{i=4}^{9} P_i \delta_i)_s}, \tag{13}$$

where δ is the mean groundwater isotope composition and sums are calculated for all winter and summer months on record.

The long term seasonal infiltration ratio α can now be used to estimate the seasonally weighted composition of recharge. This estimate has been done in variety of manners. The simplest and most common method is to use equation 12 to calculate the seasonally weighted annual average concentration. However, this limits the temporal resolution of the input function to annual steps. Interpretation of the high resolution sampling isotopic composition could provide information at sub-annual timescales, requiring a higher resolution input function. In this paper, seasonally weighted annual average precipitation along with three plausible monthly resolution input functions are investigated. The first and simplest high resolution input function is simply the precipitation record, which inherently assumes $\alpha = 1$. The second infiltration function, taken from Zuber and Maloszewski (2001), is:

$$\delta_{in}(t) = \bar{\delta} + \alpha_i P_i (\delta_I - \bar{\delta}) / \sum_{i=1}^{12} \alpha_i P_i / n, \tag{14}$$

where $\bar{\delta}$ is the mean input (which must equal the mean output) and $\alpha_i = 1$ when $10 \geq i \leq 3$ and $\alpha_i = \alpha$ otherwise. We also develop another weighting function very close in form to equation 14:

$$\delta_{in}(t) = \bar{\delta} + \alpha_i P_i(\delta_I - \bar{\delta}) / \sum_{i=1}^{12} \alpha_i P_i. \quad (15)$$

The subtle difference between equations 14 and 15 is in the normalization term. Equation 14 is normalized by the average monthly recharge, thus recharge events greater than the average monthly recharge have much larger isotope shifts; however, this results in large fluctuations of the isotope composition when the precipitation is above the monthly average, and probably underestimates mixing in the vadose zone. Conversely, equation 15 is normalized by the total annual precipitation, which means that only months which comprise a significant amount of the total seasonally weighted total annual recharge can cause deviation from the seasonally weighted annual average recharge. This function produces a very smooth infiltration function very close to the seasonally weighted average concentration, but does allow large precipitation events to modify the input signal.

3.3 STUDY AREA

The study location is a water supply tunnel which connects Josefuv dul reservoir with a water supply tunnel through the Jizera mountains in the northern Czech Republic. The tunnel is excavated through crystalline granitic rocks of the Krkonose-Jizera Composite Massif, a part of the Bohemian Massif of central Europe. The 2,600m tunnel was excavated in 1980-1981 with a maximum depth 200m below land surface (Figure 1). The tunnel has been utilized as a natural analogue underground laboratory for understanding fracture ow by the Czech radioactive waste disposal research group, RAWRA, since 2003.

Detailed geological history of the massif and characterization of the fracture network intersecting the tunnel are given in Zak et al (2009). The ~1000 km^2 Krkonose-Jizera Plutonic Complex is dominated by the Jazira and Liberec coarse-grained porphyritic biotite granodiorite to granite. The tunnel lies in the Jaziera granite which is crosscut by two sets of steeply dipping roughly orthogonal fracture sets trending NE-SW and NW-SE. Fractures are roughly planar and subparallel and show little interaction with each other. Fracture spacing ranges from 1 cm to several meters with the most common spacing between 10 cm - 120 cm. Most fractures do not transmit measurable water discharge.

Fracture discharge and isotopic composition data were collected by the Technical University of Liberec and Czech Technical University in Prague respectively from 2010 to 2014 as part of the RAWRA characterization project. These data were made available as part of the DECOVALEX 2015 project as part of a task to model ow and transport in fractured crystalline systems. Historical isotope composition of precipitation is available by leveraging the Uhlriska experimental watershed isotopes in precipitation database.

3.4 FIELD AND ANALYTICAL METHODS

Measurement of fracture discharge, water quality and temperature were at the sampling locations depicted in Figure 1. The irregularly spaced sampling intervals were chosen to be representative of different ow regimes in the tunnel (Figure 1). Manual measurements of fracture discharge were made at each site at 14 day intervals starting in 2006. Fracture discharge was

measured using V-notch weirs or drip counting depending on the fracture discharge. Automatic measurements of fracture discharge at hourly intervals began in 2009. The locations of automatic measurement have continuously expanded since 2009, thus the density of data and sampling intervals vary for each sampling site. Automated measurements are verified by manual measurements at the 14 day intervals.

Stable isotope composition of fracture discharge at the sampling sites has been measured since 2010. Stable isotope samples were collected at 14 day intervals in 50 ml bottles and analyzed at the IAEA stable isotope laboratory in Vienna, Austria. Dissolved CFC's, tritium and dissolved noble gases were measured at the IAEA Isotope Hydrology Laboratory as part of an IAEA Technical Cooperation Project. Dissolved CFCs were collected in 250 ml glass bottles with metal caps completely submerged in buckets filled with fracture discharge. Dissolved CFC concentrations were measured using purge and trap gas chromatography. Tritium was collected in 1L bottles and analyzed by electrolytic enrichment and counting. Dissolved noble gases were collected using copper tube samples (Weiss, 1968) and analyzed using mass spectrometry.

3.5 MODELLING METHODS

The input concentration history $C_{in}(t)$ was estimated at the site for each tracer modeled. Stable isotopes in precipitation near the study site are available from the Uhlriska experimental watershed at monthly internals beginning in 2006. In order to extend the precipitation data set back in time, the Vienna stable isotope in precipitation data set, the closest and longest time series in the IAEA Global Network of Isotopes in Precipitation was used to provide an estimate of the values in precipitation at the site from 1960 to 2006.

The seasonal recharge coefficient α was calculated for each modeled location using the average δD and $\delta^{18}O$ composition of the groundwater and average of Uhlriska dataset and using equation 13 to calculate an α for each isotope. The α used to create the seasonally weighted recharge concentration was taken the average of that calculated with each isotope. Seasonally weighted concentrations were then calculated for tritium, δD and $\delta^{18}O$ using raw historical precipitation and equations 12, 14 and 15 for each sampling site at monthly intervals. The input history for CFCs was calculated using the historical CFC mixing ratios in the atmosphere (Bullister, 2011), the average noble gas recharge temperature estimate of 4.8 ^{o}C from IAEA tritium-helium analyses, a characteristic recharge elevation of 750 m, and zero excess air, to give the CFC concentration at each site in biannual intervals. In order to provide high enough temporal resolution to reduce numerical error the time were resampled at daily intervals using linear interpolation to give the discrete concentration input history $\bar{C}_{in}$.

Equations 1- 10 were simulated using discrete convolution of linearly interpolated concentration input history ($\bar{C}_{in}$) and weighting function vectors ($\bar{g}$). Numerically efficient discrete convolution was accomplished using multiplication of the Fourier transformed discrete vectors. Convolution operations were written in python.

Three of the sampling locations depicted in Figure 1 representative of: shallow high discharge (V6), deep low-discharge fracture discharge (V3), and deep large discharge (V4) were modeled. The concentration in discharge was modeled at each location using equations 1 with the dispersion and exponential weighting functions and 10 with the dispersion advective travel

time distribution. At each modeled location, three different concentration input histories were evaluated (equations 12, 14 and 15) using the methods described above.

For each combination of weighting function and historical concentration history, the best fit mean groundwater age at a sampling site was estimated by fitting the observed multi-tracer data at the site. Best fit estimation was accomplished by minimizing error weighted chi-squared residual using a Levenberg-Marquardt algorithm. The error mean age estimate was calculated from the 95% confidence interval of the covariance matrix, using the Jacobian of the error weighted chi-squared residual.

3.6 RESULTS

The best fit modeled age, uncertainty estimate and χ^2 fit are reported for each precipitation weighting function for each age distribution at all modeled fracture locations in Tables 1-2. At each location, the mean age and standard deviation in estimated age for each age distribution due to the different conceptualization of seasonal recharge function is summarized in Table 4. The mean age and the standard deviation in mean age estimates due to the assumed age distribution is reported for each input function in Table 5. The effect of increasing mean travel time on $\delta^{18}O$ signal, along with the observed values at the V6 sampling site, is shown for a dispersion TTD (equation 2), using the annual average weighted precipitation function (equation 11) is shown in Figure 2. As the age increases the variation in the $\delta^{18}O$ signal decreases. The corresponding effect on the CFC-12 concentration, along with observed data for the V6 sampling site is shown in Figure 3. During the multi-tracer inversion, the difference between all the observed tracer and the modeled signal is minimized by varying the mean transit time.

Table 1 gives the summarized results for the V6 sampling site. The overall mean age for all age distributions and all recharge weighting functions is 4.58 years with a σ of 1.02 years. For the dispersive age distribution, the mean estimated age over all input functions is 3.4 years with a standard deviation (σ) of 2.6 years. The exponential age distribution gives a mean age of 5.0 years with a σ of 1.28 years for all input functions. For the matrix diffusion model, the mean total transit time is 5.33 years with a σ of 0.99 years for all input functions. In the matrix diffusion model, the mean advective travel time is 2.55 year, with an average matrix diffusion retention time of 2.78 years. The best fit to the observed data as measured by the χ^2 residual was achieved by a dispersive age distribution with the seasonal input function developed here (equation 15). The observed data and the overall best fit modeled concentration for all tracers is shown in 4. Overall, the dispersion model gives the best fits to the measured data; however, the variance in χ^2 over all the precipitation input functions is high enough to encompass the χ^2 of the matrix diffusion age distribution, indicating that it is difficult to tell the difference between the two age distributions given the uncertainty in the input function (Table 4).

Table 2 summarizes the results for the V2 sampling site. The average mean travel time (τ) over all age distributions and input functions is 7.86 years with a σ of 2.2 years. For the dispersion age distribution, the average mean travel time is 10.3 with σ of 8.49. The exponential age function gives an average mean travel time of 6.06 with a σ of 2.1 years. For the matrix diffusion distribution, the mean total transit time is 7.23 years with a σ of 2.3 years, with an average mean advective travel time of 3.3 years and an average mean retention time of 3.9 years. The best fit combination of models is the dispersion age distribution and input function 15. The

observed data and overall best fit modeled concentration for all tracers at V2 is shown in Figure 5. Overall best fits are for the dispersion model followed by the exponential and finally matrix diffusion models. The variance in χ^2 due to uncertainty in the seasonal weighting function encompasses the fits of all other travel time distributions, thus it is difficult to uniquely pick any of the travel time distributions as the best (Table 4). For the seasonal weighting functions, the overall best fit is given by the developed seasonal weighting function (equation 15). This weighting function clearly provides the best fits regardless of the travel time distribution used (Table 5).

For the V4 sampling site, the overall average mean travel time is 6.56 years with σ of 1.2 years for all travel time distributions and input functions (Table 3). Average travel time for the dispersion distribution is 5.30 years with a σ of 2.13 years. Average travel time for the exponential age distribution is 6.7 years (σ = 3.2 yr), and average travel time for matrix diffusion distribution is 7.74 (σ = 3.2 yr). For the matrix diffusion distribution the average advective mean travel time is 3.47 years and the average retention time was 4.3 years. The best fit combination was our seasonal infiltration function (eq. 15) with the dispersion equation; however, this combination produces an anomalously low mean travel time of 3.55 years. The observed data and overall best _t modeled concentration for all tracers at V4 is shown in Figure 6. The exponential age distribution fits the data nearly as well with an anomalously high mean travel time of 10.8 years. Over all the seasonal weighting functions, the best fits were given by the exponential model, followed by the dispersion model and finally the matrix diffusion model. At V4, uncertainty in the input function creates enough variance in the χ^2 residual that the average χ^2 values for each TTD are within error (Table 4), thus choosing the best age distribution is difficult given the available data. As in the other models, the input function developed in this paper provides better fits than the other input functions regardless of the travel time distribution (Table 5).

3.7 DISCUSSION

The results presented here highlight the difficulty in using tracer concentrations to constrain travel time in a fractured network system. At all sampling locations it is difficult to distinguish the best travel time distribution when considering different conceptualizations of the seasonally weighted input function. The inability to distinguish a single best age distribution using measured tracer concentration is consistent with the findings of McCallum et al (2014) and Solomon et al (2010). Thus, the estimated mean age is dependent upon the conceptualization of the system. The standard error of the mean travel time estimate (defined as the standard deviation of mean travel times normalized by the average mean travel time) over all travel time distributions and seasonal weighting input functions ranges from 19% at the V4 sampling site to 22.4% at the V6 sampling site. These results indicate that tracer derived mean travel times converge to a similar value consistent with Solomon et al (2010), and can still be used to provide significant constraint on the flow system.

A significant finding of this study is that the estimated mean travel time is as sensitive to the assumed seasonal input function as the travel time distribution. The effect of seasonality of recharge on the age estimate is largely unconsidered in most studies, and these results show that it is at least as important as the age distribution assumption. Seasonality of recharge may not have as large an effect on travel time estimates which use dissolved gas tracers when the

recharge zone is deep enough to keep the recharge temperature constant. However, in situations where the water table is shallow and seasonality is pronounced, recharge temperatures can differ from the mean annual temperature (Thoma et al, 2011) and seasonality will affect dissolved gas tracers. For isotopes of water including tritium and thus tritium-helium age dating, seasonality of recharge will always be important. Mixing of recharging waters during infiltration is a classic and active question in hydrology (e.g. Evaristo et al (2015); Kennedy et al (1986)), and more investigation is needed on the effect of seasonality on groundwater age determination. Of the seasonal recharge functions considered in this study, the developed formula consistently fits the observed data better than other functions. This function keeps the recharge concentration close to the annual average concentration, but allows large isotopic deviations in precipitation to effect the recharge concentration. While considerably more investigation is needed to validate this recharge function, the good fits here indicate that at least in this setting it appears give a reasonable approximation to the processes involved.

For two of the three model locations V6 and V2, the observed concentration was best fit by the dispersion travel time distribution. These sampling locations correspond to the discharge from individual fractures intersecting the tunnel at different depths. The shallowest sampling location V6 had the shortest travel time and the deeper sampling location, V2, had a longer travel time. The lumped parameter modeling is conceptually consistent with discharge from these fractures occurring a single fracture network, described a single ow path, rather a collection of multiple ow paths which mix together. For one of the locations, V4, the exponential age distribution fits the data as well as the dispersion model. At this location discharge from a larger fault system was sampled, thus a mixture of different ow paths with a range of ages (which the exponential model represents) is a likely conceptual model. However, uncertainty in the seasonal weighting function makes it difficult to identify which of these transit time distribution best fits the data.

The fact that the matrix diffusion model does not significantly improve fits indicates that, given the travel times in this fracture network and representative parameters controlling matrix diffusion, matrix diffusion is not a dominant process controlling transport in these fractures. The lack of significant matrix diffusion is also highlighted by the relatively small difference between the mean transport time including matrix diffusion and the mean advective only travel time (Tables 1-2). While the effect of matrix diffusion appears small on the mean travel time in this study, we expect that matrix diffusion would play a much stronger role in controlling the initial arrival and tailing properties of the transit time distribution, which are likely not identifiable using tracer concentrations (McCallum et al, 2014). Additionally, in environments with stronger matrix diffusion (e.g. high matrix porosity and/or longer travel times), the matrix diffusion transit time distribution developed here will be useful in modeling the total transit time.

3.8 CONCLUSION

We investigate the transit time distribution in fracture networks discharging to individual fractures of the Bedrichov Tunnel in the Czech Republic using time series of stable isotopes of water and tritium along with synoptic dissolved CFC concentrations. We use lumped parameter models to compare some likely transit time distributions and determine the effect of transit time distribution and seasonal input choice on the estimated mean age. We compare residence time distribution for a single advective path with longitudinal dispersion, complete mixing

(exponential age distribution) and a newly developed a residence time distribution for 1D advective-dispersive transport with infinite matrix diffusion. In order to investigate the effect of seasonal recharge, we compare uniform infiltration, a weighting function developed in Zuber and Maloszewski (2001), and a weighting function developed in this paper. We find that the modeled concentrations are dependent upon the transit time distribution and the seasonal infiltration weighting function, and that the estimated mean travel time is as sensitive to the choice of seasonal weighting function as that of the transit time distribution. Given the uncertainty in the seasonal weighting function, it is difficult to completely identify the best fit transit time distribution. However, regardless of the age distribution or the infiltration model chosen, the best fit mean age converges to a similar value for all three locations modeled here. These results indicate that lumped parameter models along with multiple environmental tracers can be used constrain the mean age, and develop some information on the transit time distribution to help develop conceptual models of ow and transport in fracture networks. The results and methods presented should be applicable in other fractured crystalline environments.

3.9 REFERENCES

Bullister JL (2011) Atmospheric CFC-11, CFC-12, CFC-113, CCl4 and SF6 Histories. Tech. rep., Carbon Dioxide Information Analysis Center, Oak Ridge National Laboratory, US Department of Energy, Oak Ridge, Tennessee, URL http://cdiac.ornl.gov/ftp/oceans/CFC ATM Hist/.

Cook P, Herczeg AL (eds) (2000) Environmental Tracers in Subsurface Hydrology. Kluwer Academic, Norwell, Massachusetts Cook P, Robinson N (2002) Estimating groundwater recharge in fractured rock from environmental H-3 and Cl-36, Clare Valley, South Australia. Water Resourses Research 38(8), DOI 10.1029/2001WR000772.

Cook P, Love A, Robinson N, Simmons C (2005) Groundwater ages in fractured rock aquifers. Journal of Hydrology 308(1-4): 284-301, DOI 10.1016/j.jhydrol.2004.11.005, URL http://www.sciencedirect.com/science/article/pii/S0022169404005360.

Danckwerts P (1953) Continuous ow systems. Chemical Engineering Science 2(1):1-13, DOI http://dx.doi.org/10.1016/0009-2509(53)80001-1, URL http://www.sciencedirect.com/ science/article/pii/0009250953800011.

Doyon B, Molson JW (2012) Groundwater age in fractured porous media: Analytical solution for parallel fractures. Advances in Water Resources 37: 127-135, DOI http://dx.doi.org/ 10.1016/j.advwatres.2011.11.008, URL http://www.sciencedirect.com/science/article/pii/ S030917081100220X

Evaristo J, Jasechko S, McDonnell JJ (2015) Global separation of plant transpiration from groundwater and stream flow. Nature 525(7567):91-94, URL http://dx.doi.org/10.1038 /nature14983.

Gardner WP, Susong DD, Solomon DK, Heasler HP (2010) Snowmelt hydrograph interpretation: Revealing watershed scale hydrologic characteristics of the Yellowstone Volcanic Plateau. Journal of Hydrology 383(3-4):209{222, DOI DOI: 10.1016/j.jhydrol.2009.12.037, URL http://www.sciencedirect.com/science/article/ B6V6C-4Y34R3F4/2/7600ad03d1d63fefa58766bc7aa7d0b3.

Gardner WP, Susong DD, Solomon DK, Heasler HP (2011) A multitracer approach for characterizing interactions between shallow groundwater and the hydrothermal system in the Norris Geyser Basin area, Yellowstone National Park. Geochemistry Geophysics Geosystems 12(8): Q08,005, URL http://dx.doi.org/10.1029/2010GC003353.

Haggerty R, Gorelick SM (1995) Multiple-rate mass transfer for modeling diffusion and surface reactions in media with pore-scale heterogeneity. Water Resources Research 31(10):2383-2400, URL http://dx.doi.org/10.1029/95WR10583.

Haggerty R, McKenna SA, Meigs LC (2000) On the late-time behavior of tracer test breakthrough curves. Water Resources Research 36(12):3467-3479, URL http://dx.doi.org/10.1029/2000WR900214.

Haggerty R, Fleming SW, Meigs LC, McKenna SA (2001) Tracer tests in a fractured dolomite: 2. analysis of mass transfer in single-well injection-withdrawal tests. Water Resources Research 37(5):1129-1142, URL http://dx.doi.org/10.1029/2000WR900334.

Kennedy V, Kendall C, Zellweger G, Wyerman T, Avanzino R (1986) Determination of the components of stormow using water chemistry and environmental isotopes, Mattole river basin, California. Journal of Hydrology 84(12):107-140, DOI http://dx.doi.org/10.1016/0022-1694(86)90047-8, URL http://www.sciencedirect.com/science/article/pii/0022169486900478.

Maloszewski P, Zuber A (1982) Determining the turnover time of groundwater systems with the aid of environmental tracers. Journal of Hydrology 57(3):207-231, DOI http://dx.doi.org/10.1016/0022-1694(82)90147-0, URL http://www.sciencedirect.com/science/article/pii/ 0022169482901470

Maloszewski P, Zuber A (1985) On the theory of tracer experiments in fissured rocks with a porous matrix. Journal of Hydrology 79(3):333-358, DOI http://dx.doi.org/10.1016/0022-1694(85)90064-2, URL http://www.sciencedirect.com/science/article/pii/0022169485900642.

Maloszewski P, Zuber A (1990) Mathematical modeling of tracer behavior in short-term experiments in fissured rocks. Water Resources Research 26(7):1517-1528, DOI 10.1029/WR026i007p01517, URL http://dx.doi.org/10.1029/WR026i007p01517.

Maloszewski P, Zuber A (1996) Lumped parameter models for the interpretation of environmental tracer data. IAEA Technical Report.

McCallum JL, Engdahl NB, Ginn TR, Cook PG (2014) Nonparametric estimation of groundwater residence time distributions: What can environmental tracer data tell us about groundwater residence time? Water Resources Research DOI 10.1002/2013WR014974, URL http://dx.doi.org/10.1002/2013WR014974.

Neretnieks I (1980) Di_usion in the rock matrix: An important factor in radionuclide retardation? Journal of Geophysical Research: Solid Earth 85(B8):4379-4397, DOI 10.1029/JB085iB08p04379, URL http://dx.doi.org/10.1029/JB085iB08p04379.

Neretnieks I (1981) Age dating of groundwater in fissured rock: Influence of water volume in micropores. Water Resources Research 17(2):421{422, DOI 10.1029/WR017i002p00421, URL http://dx.doi.org/10.1029/WR017i002p00421.

Neuman S (2005) Trends, prospects and challenges in quantifying flow and transport through fractured rocks. Hydrogeology Journal 13(1):124-147, DOI 10.1007/s10040-004-0397-2, URL http://dx.doi.org/10.1007/s10040-004-0397-2.

Painter S, Cvetkovic V (2005) Upscaling discrete fracture network simulations: An alternative to continuum transport models. Water Resoures Research 41(2):W02,002, URL http://dx.doi.org/10.1029/2004WR003682.

Painter S, Cvetkovic V, Mancillas J, Pensado O (2008) Time domain particle tracking methods for simulating transport with retention and first-order transformation. Water Resoures Research 44(1): W01,406, URL http://dx.doi.org/10.1029/2007WR005944.

Roubinet D, de Dreuzy JR, Tartakovsky DM (2013) Particle-tracking simulations of anomalous transport in hierarchically fractured rocks. Computers & Geosciences 50:52-58, DOI http://dx.doi.org/10.1016/j.cageo.2012.07.032, URL http://www.sciencedirect.com/ science/ article/pii/S0098300412002774, benchmark problems, datasets and methodologies for the computational geosciences.

Shapiro AM (2001) Effective matrix diffusion in kilometer-scale transport in fractured crystalline rock. Water Resources Research 37(3):507{522, DOI 10.1029/2000WR900301, URL http://dx.doi.org/10.1029/2000WR900301.

Solomon DK, Genereux DP, Plummer LN, Busenberg E (2010) Testing mixing models of old and young groundwater in a tropical lowland rain forest with environmental tracers. Water Resour Res 46(4): W04,518, URL http://dx.doi.org/10.1029/2009WR008341.

Solomon DK, Gilmore TE, Solder JE, Kimball B, Genereux DP (2015) Evaluating an unconfined aquifer by analysis of age-dating tracers in stream water. Water Resources Research 51(11):8883{8899, DOI 10.1002/2015WR017602, URL http://dx.doi.org/ 10.1002 /2015WR017602.

Sudicky EA, Frind EO (1982) Contaminant transport in fractured porous media: Analytical solutions for a system of parallel fractures. Water Resources Research 18(6):1634{1642, DOI 10.1029/WR018i006p01634, URL http://dx.doi.org/10.1029/WR018i006p01634.

Tang DH, Frind EO, Sudicky EA (1981) Contaminant transport in fractured porous media: Analytical solution for a single fracture. Water Resources Research 17(3):555-564, DOI 10.1029/WR017i003p00555, URL http://dx.doi.org/10.1029/WR017i003p00555.

Therrien R, Sudicky E (1996) Three-dimensional analysis of variably-saturated flow and solute transport in discretely-fractured porous media. Journal of Contaminant Hydrology 23(1-2):1-44, DOI 10.1016/0169-7722(95)00088-7, URL http://www.sciencedirect.com /science/article/pii/0169772295000887.

Thoma MJ, McNamara JP, Gribb MM, Benner SG (2011) Seasonal recharge components in an urban/agricultural mountain front aquifersystem using noble gas thermometry. Journal of Hydrology 409(12):118-127, DOI http://dx.doi.org/10.1016/j.jhydrol.2011.08.003, URL http://www.sciencedirect.com/science/article/pii/S0022169411005294.

Warren J, Root P (1963) The behavior of naturally fractured reservoirs. Society of Petroleum Engineers 228:245-255.

Weiss R (1968) Piggyback sampler for dissolved gas studies on sealed water samples. Deep Sea Research and Oceanographic Abstracts 15(6):695-699.

Zak J, Verner K, Klominsky J, Chlupacova M (2009) \Granite tectonics" revisited: insights from comparison of K-feldspar shape-fabric, anisotropy of magnetic susceptibility (AMS), and brittle fractures in the Jizera granite, Bohemian Massif.nternational Journal of Earth Sciences 98(5):949-967.

Zuber A, Maloszewski P (2001) Environmental Isotopes in the Hydrologic Cycle, IHP-V Technical Documents in Hydrology, vol 6. International Atomic Energy Agency.

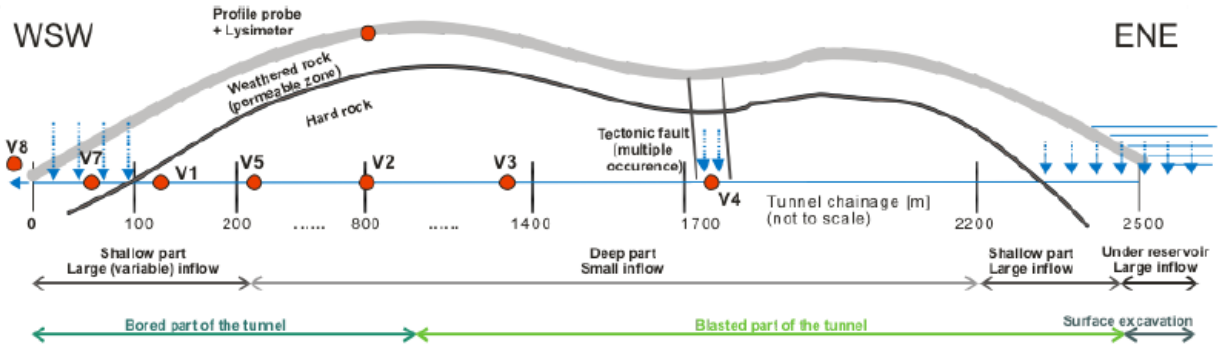

Fig. 1: Schematic cross-section and profile of the Bedrichov Tunnel along with technical and hydrological conditions.

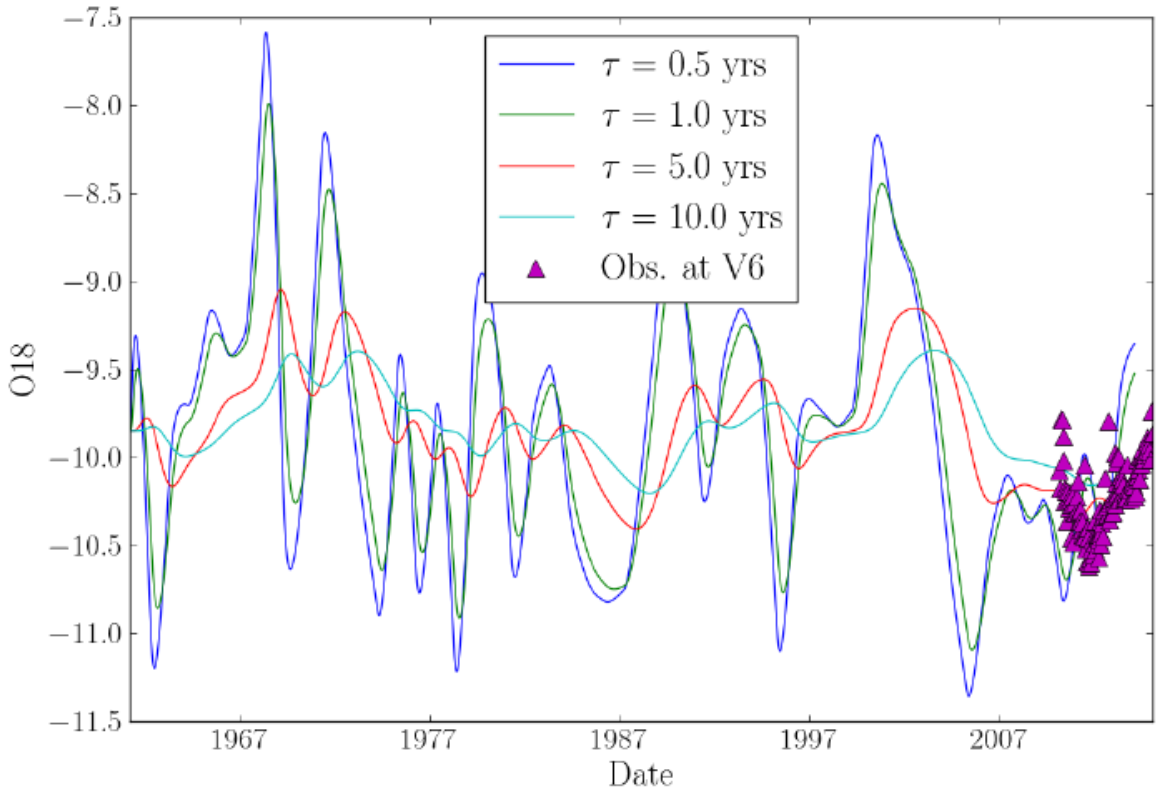

Fig. 2: Effect of increasing mean travel time on the modeled $\delta^{18}O$ signal using the annual average weighting function and the dispersion TTD for the V6 sampling site along with the observed $\delta^{18}O$ signal.

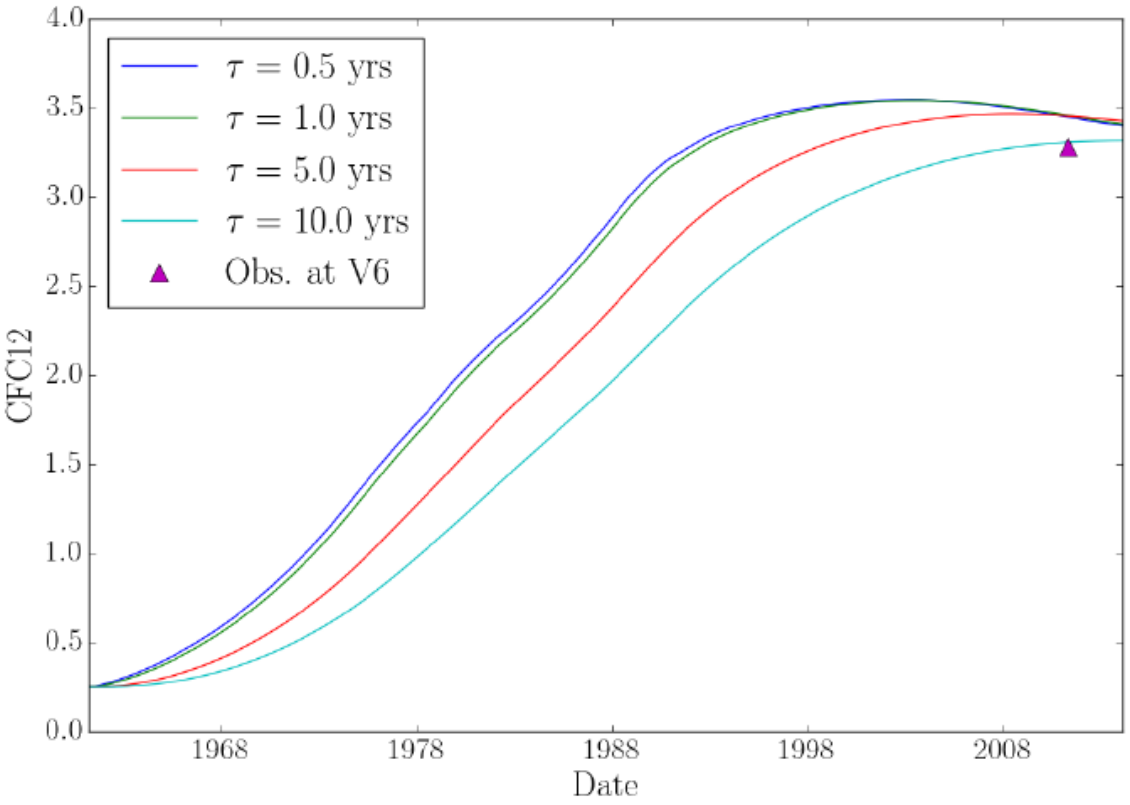

Fig. 3: Effect of increasing mean travel time on the modeled CFC-12 signal using the annual average weighting function and the dispersion TTD for the V6 sampling site along with the observed CFC concentration.

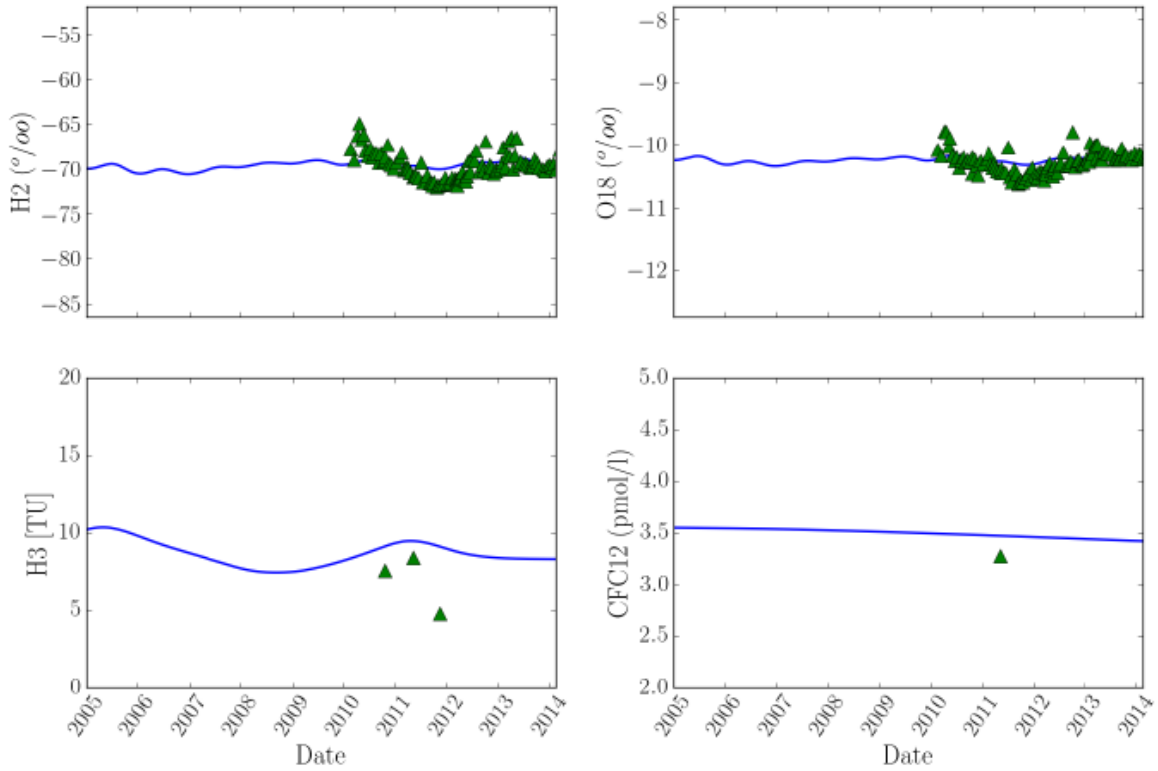

Fig. 4: Tracer data at the V6 sampling location, and the overall multi-tracer best fit lumped parameter model results. For V6 the best fit was achieved for a dispersion TTD using the seasonal input function derived in equation 15.

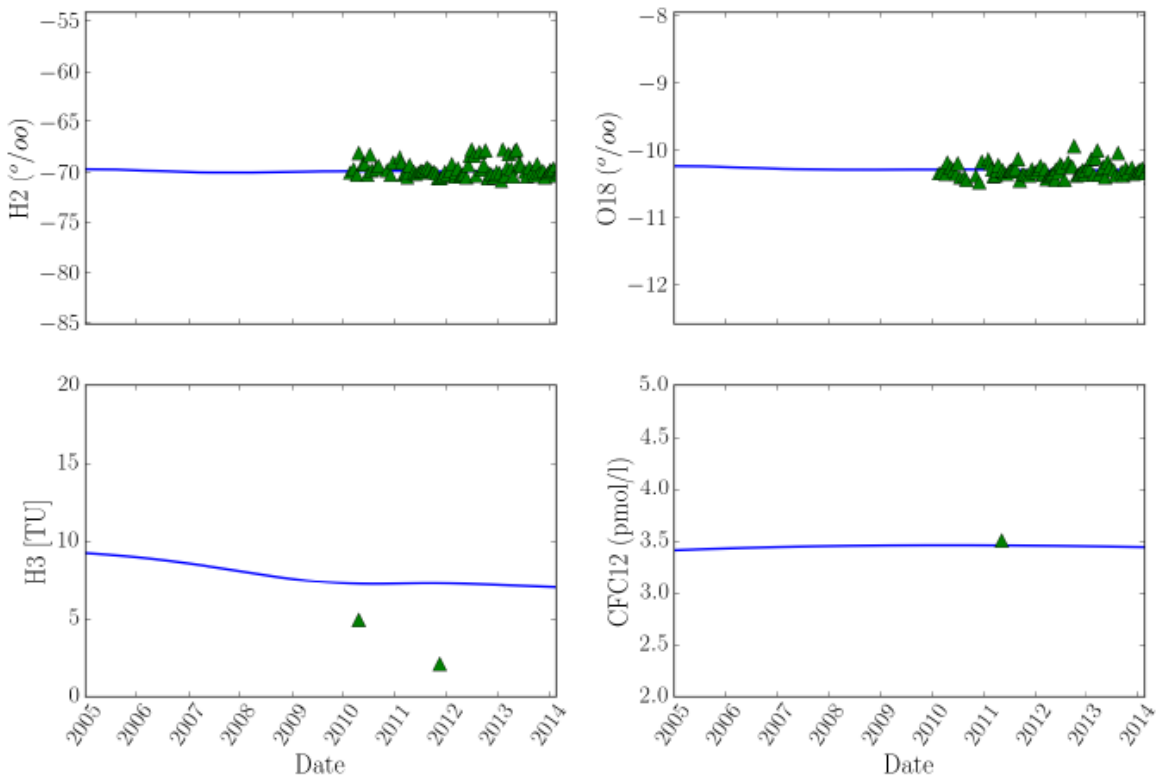

Fig. 5: Tracer data at the V2 sampling location, and the overall multi-tracer best fit lumped parameter model results. For V2 the best fit was achieved for a dispersion TTD using the seasonal input function derived in equation 15.

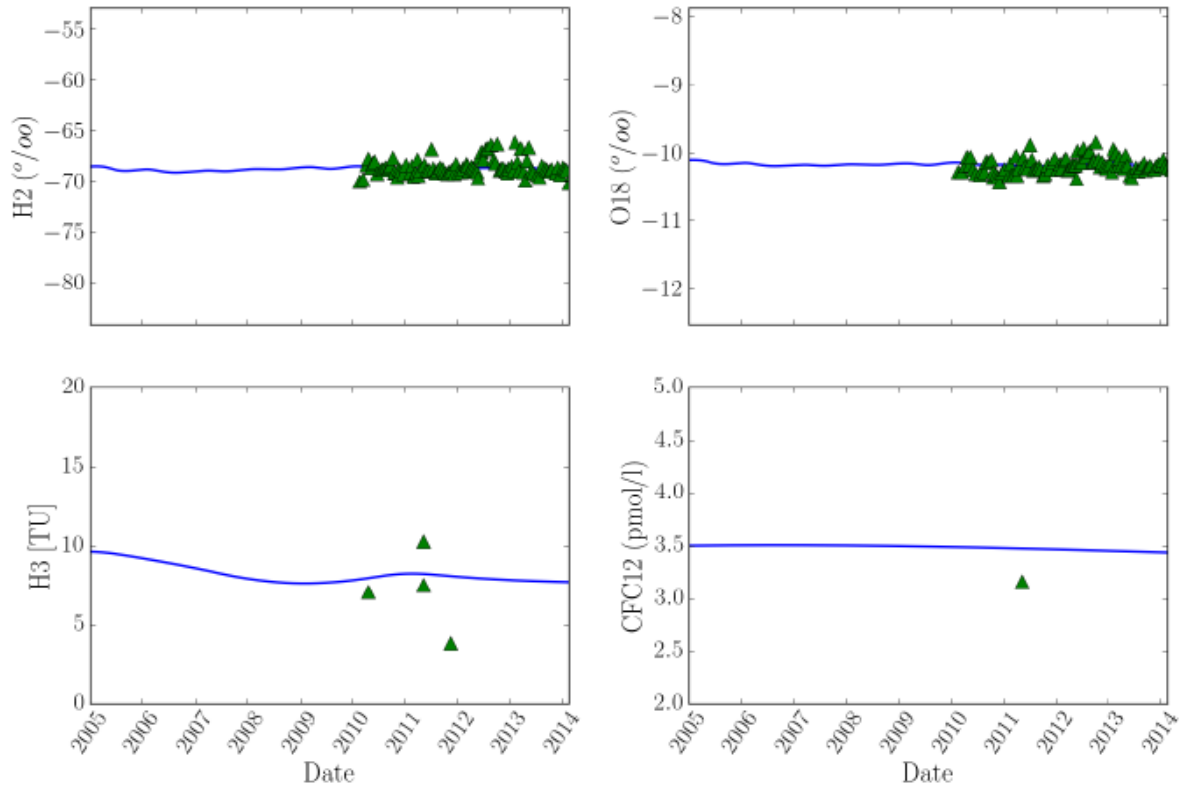

Fig. 6: Tracer data at the V4 sampling location, and the overall multi-tracer best fit lumped parameter model results. For V4 the best fit was achieved for a dispersion TTD using the seasonal input function derived in equation 15.

Table 1: Summary results for V6 sampling site

Age Distriubtion ($g(t)$)	Infil. Func. ($C_{in}(t)$)	τ_{adv} (yr)	+/- (yr)	χ^2	τ_{tran} yr
Dispersive-Matrix Diffusion	Uniform	2.31	0.09	573	4.73
	eq. 11	3.09	0.31	299	6.67
	eq. 14	2.62	0.15	240	5.49
	eq. 15	2.19	0.65	200	4.45
Dispersive	Uniform	2.65	0.1	343	–
	eq. 11	7.17	0.73	283	–
	eq. 14	2.58	0.15	189	–
	eq. 15	1.27	0.14	177	–
Exponential	Uniform	3.1	0.18	651	–
	eq. 11	5.64	0.44	328	–
	eq. 14	5.78	0.55	382	–
	eq. 15	5.5	0.46	317	–

Table 2: Summary results for V2 sampling site

Age Distriubtion ($g(t)$)	Infil. Func. ($C_{in}(t)$)	τ_{adv} (yr)	+/- (yr)	χ^2	τ_{tran} yr
Dispersive-Matrix Diffusion	Uniform	2.57	0.13	575	5.37
	eq. 11	4.56	0.32	214	10.6
	eq. 14	2.83	0.2	272	6.03
	eq. 15	3.22	1.95	107	6.99
Dispersive	Uniform	3.13	0.14	445	
	eq. 11	8.22	0.93	202	
	eq. 14	7.32	1.07	250	
	eq. 15	6.65	5.4	108	
Exponential	Uniform	3.07	0.18	466	
	eq. 11	7.72	0.7	226	
	eq. 14	6.66	0.77	303	
	eq. 15	6.81	6	111	

Table 3: Summary results for V4 sampling site

Age Distriubtion ($g(t)$)	Infil. Func. ($C_{in}(t)$)	τ_{adv} (yr)	+/- (yr)	χ^2	τ_{tran} yr
Dispersive-Matrix Diffusion	Uniform	2.22	0.09	407	4.53
	eq. 11	4.49	0.16	210	10.4
	eq. 14	2.55	0.15	265	5.34
	eq. 15	4.62	0.22	101	10.7
Dispersive	Uniform	3.27	0.18	372	
	eq. 11	7.08	0.76	182	
	eq. 14	7.13	0.97	242	
	eq. 15	3.55	1.3	96.3	
Exponential	Uniform	3.15	0.18	292	
	eq. 11	7.24	0.62	224	
	eq. 14	5.62	0.54	271	
	eq. 15	10.8	1.94	99.7	

Table 4: Average mean age and standard deviation of mean age estimate for all seasonal input functions given a TTD at each sample location

Model	Input func.	τ_{adv} (yr)	σ (yr)	$\bar{\chi}^2$	σ_χ
V6	Dispersive-Matrix Diffusion	5.33	0.993	328	168
	Dispersive	3.42	2.58	248	79.1
	Exponential	5	1.28	420	157
V2	Dispersive-Matrix Diffusion	7.24	2.31	292	201
	Dispersive	6.31	2.22	251	142
	Exponential	6.06	2.05	276	149
V4	Dispersive-Matrix Diffusion	7.74	3.26	246	127
	Dispersive	5.26	2.14	223	116
	Exponential	6.7	3.21	222	86.1

Table 5: Average mean age and standard deviation of mean age estimate for all TTDs given the seasonal input function at each sample location

Model	Input func.	τ_{adv} (yr)	σ (yr)	$\bar{\chi}^2$	σ_χ
V6	Uniform	3.49	1.09	522	160
	eq. 11	6.49	0.78	303	22.8
	eq. 14	4.62	1.77	270	100
	eq. 15	3.74	2.2	231	75.1
V2	Uniform	3.86	1.31	495	69.8
	eq. 11	8.83	1.52	214	12
	eq. 14	6.67	0.645	275	26.6
	eq. 15	6.82	0.17	109	2.08
V4	Uniform	3.65	0.764	357	58.9
	eq. 11	8.23	1.85	205	21.4
	eq. 14	6.03	0.963	259	15.3
	eq. 15	8.36	4.17	99	2.43

4. STREAMING POTENTIAL TEST: FINAL REPORT

4.1 INTRODUCTION

Generally, fluid flow in a porous medium and then the drag of excess charge in an electrical double layer at solid-fluid interface introduce a streaming current, and the associated electrical potential is a streaming potential (SP) (Lorne et al., 1999). The SP measurement is one of the oldest methods in geophysical techniques. It consists of monitoring electrical field existing at the ground surface of the earth where the SP signals provide the evidence of polarization mechanisms existing in the grounds. The use of the SP in different aspect of geology has been developed for the last two decades and these methods have been used for a variety of geophysical applications to detect and monitor water flow (e.g., Blake and Clarke, 1999) and leakage zones of dam (e.g., Bogoslovsky and Ogilvy, 1970; Titovet al., 2000). The SP was also used to detect the ore bodies and contaminant plumes that are rich in organic matter associated with the electro redox effect (e.g., Arora et al., 2007; Jardani et al., 2008). Because the SP is directly occurred by the hydraulic gradients in porous media and is very sensitive to the actual water, however, the major contribution of SP has been to characterize fully or partially saturated media (e.g., Fournier, 1989; Mikhailov et al., 1997; Doussan et al., 2002; Suski et al., 2004; Revil et al., 2004; Jon et al., 2008).

During a hydraulic test, which is the classical method used to obtain information about the distribution of hydraulic properties of an aquifer, SP signals can be recorded at the ground surface by measuring electric potential differences between the nonpolarized electrodes by voltmeter and these electrodes are usually set up with the direction of water flow. Groundwater flows through a porous medium, and SP is changed due to excess charge of the pore water at the nearby mineral-pore water interface. The change of SP helps for detecting the fluid flow to characterize the hydraulic properties of the medium. Rizzo et al. (2004) estimated the hydraulic properties of an aquifer from hydraulic head and SP signals through numerical modeling with associated hydraulic tests. Malama et al. (2009a, 2009b) developed semi-analytical solution for transient streaming potentials associated with axial symmetric flow by pumping in the confined and unconfined aquifers.

Here we present a sandbox experiment to check the feasibility of SP to estimate solute transport characteristics of an aquifer. We conducted tracer tests under steady-state groundwater flow condition with recording SP signals. We used an acrylic tank filled with medium to coarse grained sand and infiltrated with water, and tried to detect the changes in SP signals due to injection and transport of tracer.

4.2 MATERIALS AND METHODS

Fig. 1 is the flow chart of this study. An acrylic tank was prepared for the experiment, and filled with homogeneous sand which was medium to coarse grained quartz sand with clay particles. Two reservoirs were connected to the sandbox, and they were upstream and downstream reservoirs which were used to control the water flow condition in the sandbox by overflowing water from the pipe connected to the bottom of the two reservoirs. The total length

of the acrylic tank was 2.5 m with the sandbox of 1.5 m, the upstream reservoir of 0.5 m and the downstream reservoir of 0.5 m, and its height was 1.0 m as shown in Fig. 2. The upstream and downstream reservoirs were separated from the sandbox by 200 μm stainless steel mesh. Here we used five plastic screened wells which were around 1.5 cm in diameter and 1.0 m long. These screened wells included micro holes with the diameter of 0.2 cm to infiltrate water and were covered by 200 μm plastic mesh not to fill with sand during the experiments and to collect water sample uninterruptedly (Fig. 2). The screened wells set parallel at the middle of the sandbox about 25 cm distances each other. The tops of the wells were open in the air, and bottoms were sealed into the sandbox. 20 sintered Ag/AgCl non-polarizing electrodes were installed at the top of the sand aquifer, and they surrounded the screened wells with definite distance of 8 cm to collect SP signals in the sandbox during the experiments (Crespy et al., 2008; Martinez-Pagan et al., 2010). Fig. 3 shows the setting of the instrument for the experiment.

The hydraulic conductivity of the sandbox was determined through groundwater flow tests. For the tests, the steady-state condition of groundwater flow was established by maintaining the hydraulic head difference between the upstream and downstream reservoirs. After establishing the steady-state condition, we measured the out-flow rate at the downstream of the sandbox and calculated the hydraulic conductivity using equation (1) which was from Darcy's law:

$$K = \frac{q}{Ai} \quad (1)$$

where q is the out-flow rate [m^3/sec], A is the cross sectional area of the sandbox [m^2], L is the length of the sandbox [m], H is the hydraulic head [m], and i is the hydraulic gradient given by $i = \frac{H_{upstream} - H_{downstream}}{L}$. In this study, we estimated the hydraulic conductivity with several hydraulic head differences. Using the estimated hydraulic conductivity, we simulated the tracer test for its design. From the simulation we determined the optimal injection rate and sampling intervals. In the simulation, we assumed the effective porosity and longitudinal dispersivity to 0.15 and 0.1 m, respectively, referring to Domenico and Schwartz (1990).

A tracer test was also conducted using the sandbox. NaCl solution with the concentration of 1000 ppm was used as a tracer. We injected the tracer into the second screened well for five minutes. Before and after tracer injection, water was injected to the injection well with the same injection rate to maintain the water flow condition during the whole experiment. We collected water samples from each of the five screened wells using disposable syringes, and analyzed their concentration with the chloride analyzer (Model-926, Cole-Palmer Inc.). The tracer test results were analyzed as follows. The linear velocity was calculated from the peak arrival time of the obtained breakthrough curves, and the longitudinal dispersion coefficient was introduced from the variance of the breakthrough curves using equation (2) (Fetter, 1992):

$$D_L = \frac{\sigma^2}{2t} \quad (2)$$

where D_L is the longitudinal dispersion coefficient [m^2/sec], t is the peak arrival time of the tracer [sec] and σ^2 is the variance of the breakthrough curve [m^2]. During the experiments, the change of SP signals were recorded using 20 sintered Ag/AgCl electrodes connected with a multimeter

(Model-M2700, Keithly Inc.). The multimeter was connected with the computer to collect electrical signals automatically. Fig. 4 shows the channel numbers of each electrode installed in the sandbox. Note that we considered another electrode as a reference which was located beside the sandbox.

4.3 RESULTS AND DISCUSSION

The hydraulic conductivity of the sandbox was estimated from the groundwater flow tests with various hydraulic head differences between upstream and downstream reservoirs. From equation (1), the hydraulic conductivity was calculated to $2.50 \times 10^{-4} \pm 2.09 \times 10^{-5}$m/sec. Fig. 5 is the numerical simulation results of the tracer test for test design. The results show that the injection rate of 0.005 L/sec into the second screened well and the head difference less than 5 cm were sufficient conditions for the dimension of our sandbox. They also indicated that sampling intervals of five minutes at first 2 hours and ten minutes for the rest of the test were enough to detect the breakthrough curves at each well.

The tracer test was conducted in two phases. In the first phase, a steady-state groundwater flow condition was established by maintaining the hydraulic heads at the upstream and downstream reservoirs and by injecting water into the injection well with the designed rate. In the second phase, we injected tracer instead of water for 5 minutes, and then injected water again to maintain water flow condition. The chloride concentrations of collected water samples during the experiment were plotted in Fig. 6. It shows that the tracer moved slowly from the injection well to other wells. The obtained breakthrough curves were similar to the normal distribution curve although the break-through curve from the third screened well (SW-3) showed double peaks. At the fourth (SW-4) and fifth (SW-5) screened wells, it was difficult to identify the breakthrough curve. Table 1 shows the analysis results of the tracer test. For SW-3, the first peak of the chloride concentration was analyzed to estimate the linear velocity and dispersion coefficient. Tracer analysis results show the variation of linear velocity and dispersion coefficient in different screened wells. From the injected well to the last screened well it shows natural plume was created by the tracer solution. Here, the highest linear velocity was 5.5×10^{-6} m/sec at SW-3 and the largest dispersion coefficient was 2.8×10^{-4} m^2/sec at SW-1. However, the estimated linear velocities and dispersion coefficients were similar in the order of magnitude, respectively.

Fig. 6 also shows the distributions of SP signals data set measuring during the experiment. The black dotted boxes in the graphs indicate the duration of tracer injection. We did not found any significant change of SP signal dataset before the injection of tracer but we found signals responding to solute transport at SW-1, SW-2 and SW-3. At SW-1, the chloride concentration showed one peak at 180 to 200 minutes, and during that time SP signals also showed the reverse effect. Similarly, at other screened wells, the SP signals also changed when the chloride concentration changed. These results indicate that the SP signals are likely to be related to the solute transport.

4.4 CONCLUSIONS

To evaluate the feasibility of SP signals on estimation of solute transport properties of an aquifer, we conducted a tracer test with measuring SP signals. The results confirmed that the

measured SP signals were produced during our experiment, and it showed significant trend or relationship between the SP and solute transport property of the sandbox during the whole period of experiment. However, we could not confirm this conclusion because there are few previous researches which provide the theoretical backgrounds of the observed phenomena in our experiments. Thus, further study to quantify the behavior of SP responding to solute transport is necessary.

Our results indicate a clue that there is a relation between SP and solute transport in an aquifer, which provides a stepping-stone for the expansion of our understanding of transport in an aquifer and reduction of the uncertainty in a tracer test.

4.5 REFERENCES

Arora, T., Revil, A., Linde, N., and Castermant, J., 2007, Non-intrusive determination of the redox potential of contaminant plumes using the self-potential method, *J. Contamin. Hydrol*., **92**, 274– 292.

Blake, E.W. and Clarke, G.K.C., 1999, Subglacial electrical phenomena, *J. Geophys. Res.*, **104**, 7481–7495.

Bogoslovsky, V.A. and Ogilvy, A.A., 1970, Natural potential anomalies as a quantitative index of the rate of seepage from water reservoirs, *Geophys, Prospec.*, **18**, 261–268.

Crespy, A., Revil, A., Linde, N., Byrdina, S., Jardani, A., Boleve, A., and Henry, P., 2008, Detection and localization of hydromechanical disturbances in a sandbox using the self-potential method, *J. Geophy. Res.*, **113**, B01205, doi:10.1029/2007JB005042.

Domenico, P.A. and Schwartz, F.W., 1990, *Physical and Chemical Hydrogeology*, John Wiley & Sons, New York.

Doussan, C., Jouniaux, L., and Thony, J.L., 2002, Temporal variations of SP and unsaturated water flow in loam and clay soils: a seasonal field study, *J. Hydrol*., **267**, 173-185.

Fournier, C., 1989, Spontaneous potentials and resistivity surveys applied to hydrogeology in a volcanic area: Case history of the Chaine des Puys (Puy-de-Dome, France), *Geophys. Prospec.*,**37**, 647–668.

Fetter, C.W., 1992, *Contaminant Hydrogeology*, Department of Geology, University of Wisconsin-Oshkosh.

Jardani, A., Revil, A., and Dupont, J.P., 2008, Three-dimensional inversion of self-potential data used to constrain the pattern of groundwaterflow in geothermal fields, *J. Geophys. Res.*, **113**, 1-22.

Jon, H., Saunders, L., Matthew, D., Jackson, L., and Christopher, C.P., 2008, Fluid flow monitoring in oil fields using downhole measurements of electrokinetic potential, *Geophysics*, **73**, 165-180.

Jouniaux, L., Maineult, A., Naudet. V., Pessel, M., and Sailha, P., 2009, Review of self-potential methods in hydrogeophysics, *Critical Review Geosciences*, **341**, 928-936.

Lorne, B., Perrier, F., and Avouac, J.P., 1999, Streaming potential measurements 1. Properties of the electrical double layer from crushed rock samples, *J. Geoph. Res.*, **104**, 17,857–17,877.

Maritinez-Pagan, P., Jardani, A., Revil, A., and Haas, A., 2010, Self-potential monitoring of a salt plume, *Geophysics*, **75**, WA17-WA25.

Mikhailov, O.V., Queen, J.H., and Toksoz, M.N., 1997, Using borehole electro seismic measurements to detectandcharacterize fractured (permeable)zones, *Annual Technical Report*.

Malama, B., Revil, A., and Kristopher, L.K., 2009a, Asemi-analytical solution for transient streaming potentials associated with confined aquifer pumping tests, *Geophys. J. Int*., **176**, 1007-1016.

Malama, B., Kristopher, L.K., and Revil, A., 2009b, Theory of transient streaming potentials associated with axial-symmetric flow in unconfined aquifers, *Geophys. J. Int*., **179**, 990-1003.

Revil, A., Naudet, V., and Meunier, J.D., 2004, The hydroelectric problem of porous rocks: Inversion of the position of the water table from self-potential data, *Geophys. J. Int*., **159**, 435–444.

Rizzo, E., Suski, B., Revil, A., Straface, S., and Troisi, S., 2004, Self-potential signals associated with pumping-tests experiments, *J. Geoph. Res.*, **109**, B10203.

Suski, B., Rizzo, E., and Revil, A., 2004, A sandbox experiment of self-potential signals associated with pumping test, *Vadose Zone J.*, **3**, 1193-1199.

Titov, K., Loukhmanov, V., and Potapov, A., 2000, Monitoring of water seepage from a reservoir using resistivity and self-polarization methods: Case history of the Petergoph fountain water supply system, *First Break*, **18**, 431–435.

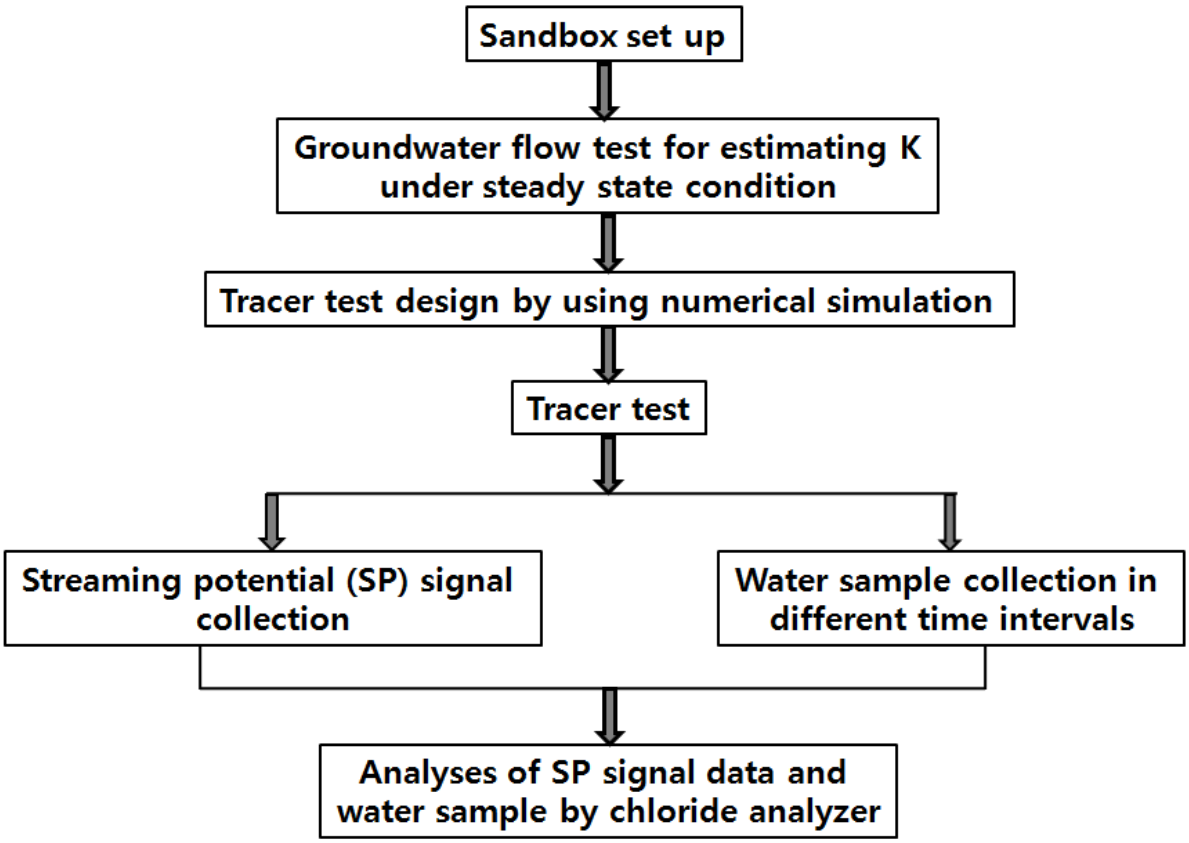

Figure 1: Flow chart of this study

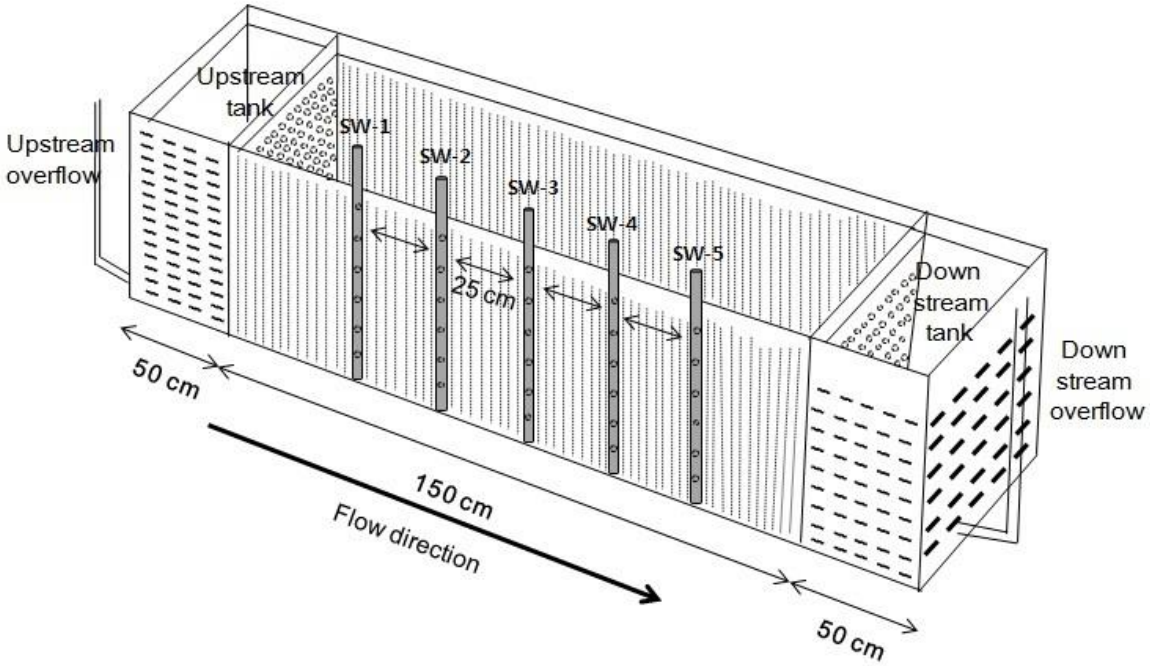
Upstream tank
Upstream overflow
SW-1
SW-2
SW-3
SW-4
SW-5
25 cm
Down stream tank
Down stream overflow
50 cm
150 cm
Flow direction
50 cm

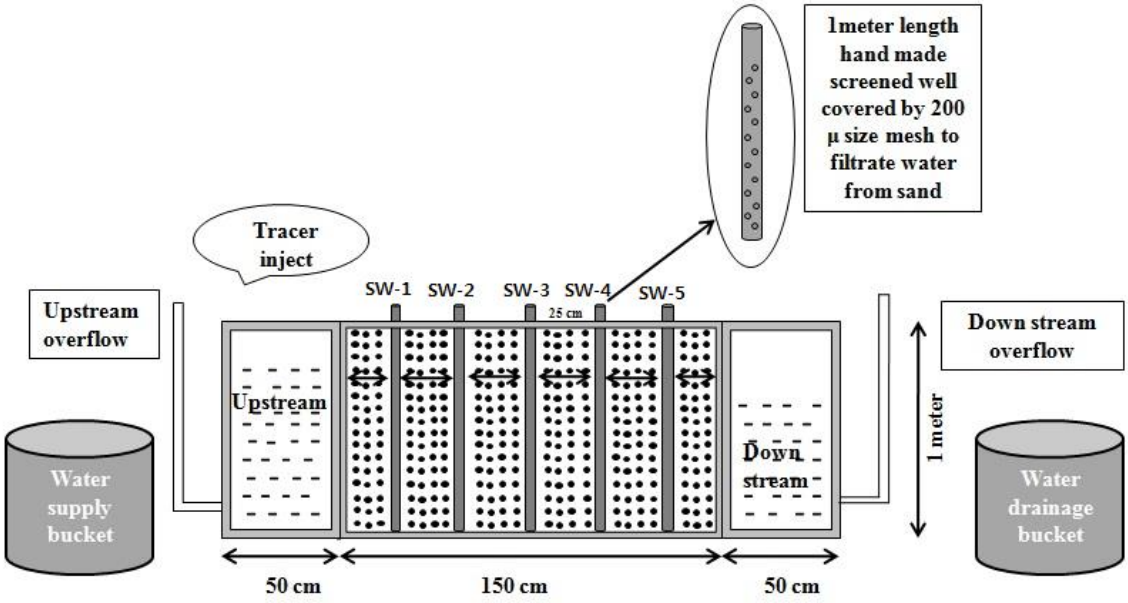
1meter length hand made screened well covered by 200 µ size mesh to filtrate water from sand
Tracer inject
SW-1
SW-2
SW-3
SW-4
SW-5
25 cm
Upstream overflow
Down stream overflow
Upstream
Down stream
1 meter
Water supply bucket
Water drainage bucket
50 cm
150 cm
50 cm

Figure 2. Design of the sandbox

Figure 3: Full set up of a sandbox experiment

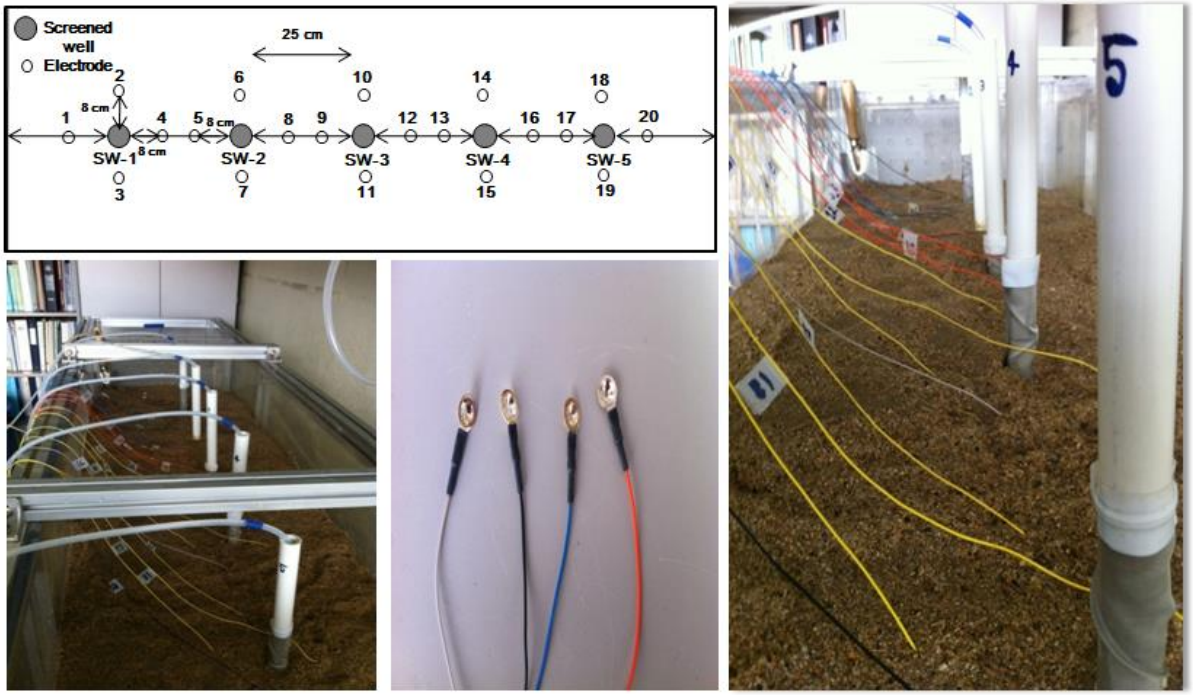

Figure 4: Electrode set up into the sandbox

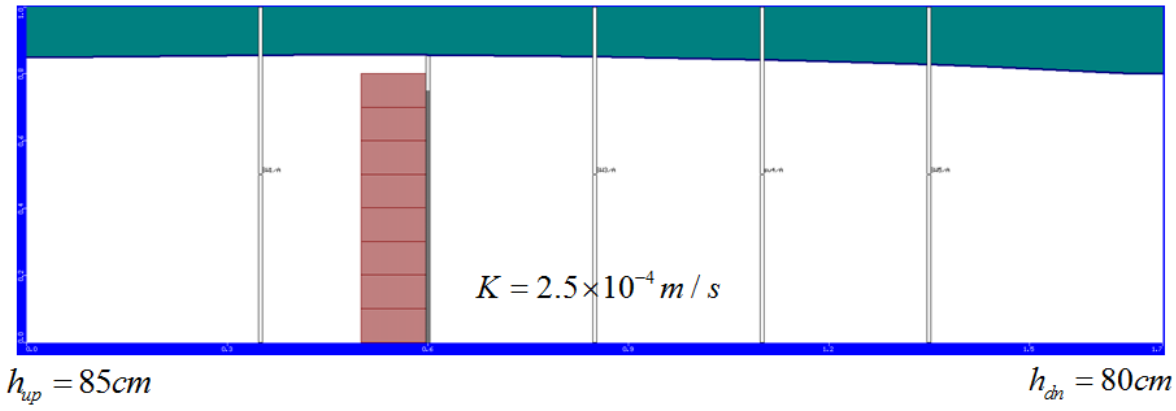

(a) Simulated water table with the injection rate of 0.005 L/sec

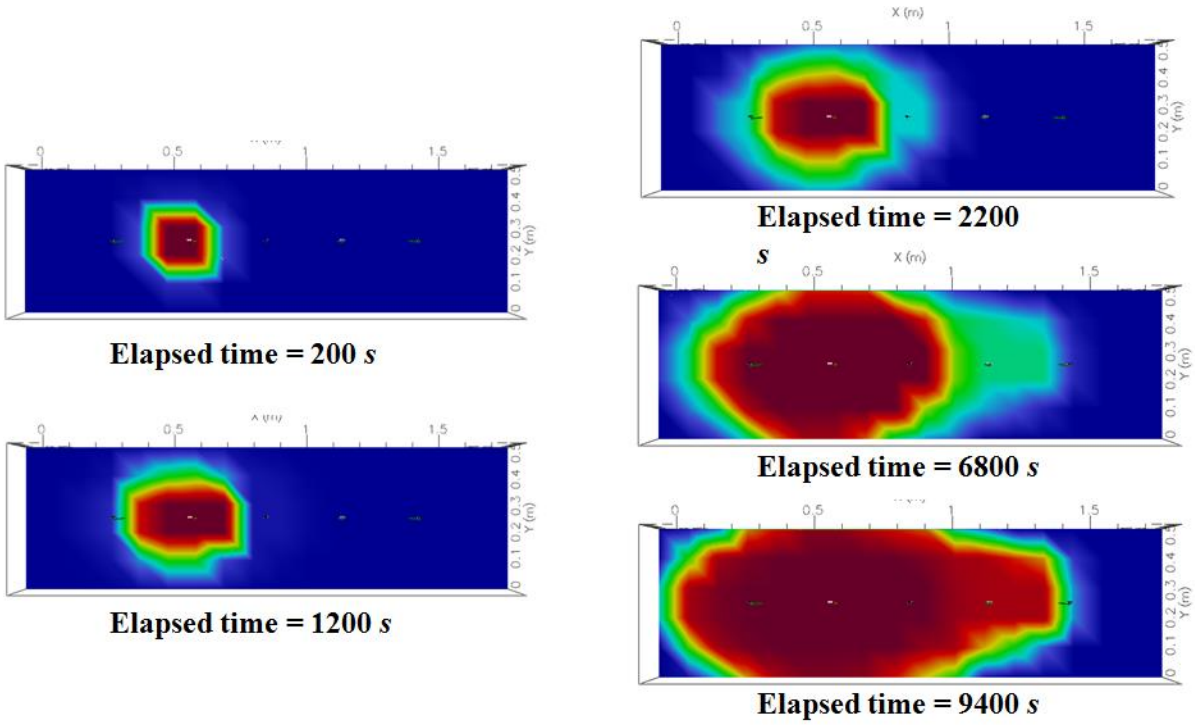

(b) Simulated tracer plume with the injection rate of 0.005 L/sec

Figure 5: Numerical simulation results of the tracer test design.

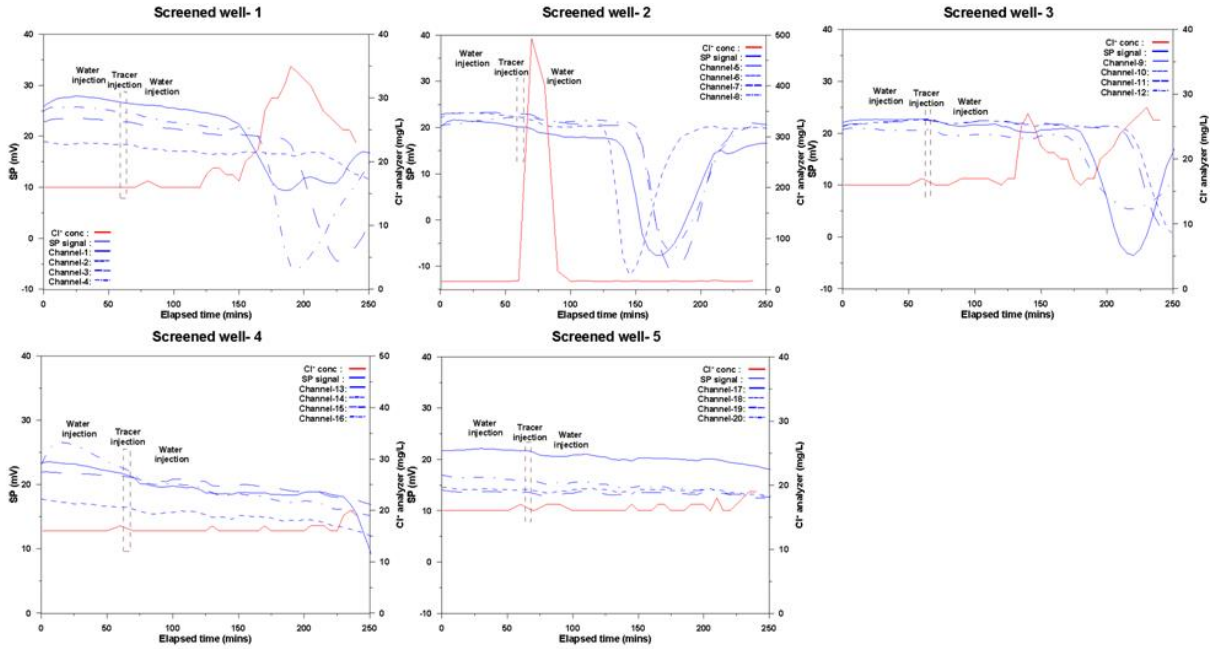

Figure 6: Measured SP signals and Cl^- concentrations during the experiment where black dotted boxes in the graph indicates timing of tracer injection.

Table 4-1: Analysis results of the tracer test.

* Not Available

Screened well	Average linear velocity, v_i (m/sec)	Hydrodynamic dispersion coefficient parallel to the direction of flow, D_L(m^2/sec)	Variance of the parallel spreading of plume, σ_L^2 (m^2)
SW-1	$3.3x10^{-6}$	$2.8\ x10^{-4}$	6.46
SW-3	$5.5x10^{-6}$	$1.4\ x10^{-4}$	4.07
SW-4	NA*	NA	NA
SW-5	NA	NA	NA

5. THERMAL-HYDROLOGIC-MECHANICAL PROPERTIES OF BUFFER MATERIALS

5.1 INTRODUCTION

KAERI has characterized the domestic Ca-bentonite in order to use it as a buffer material for the geological disposal system. In this section, the requirements of buffer and the major characteristics related to the THM behaviors are briefly described with a brief description of the geological disposal system for high-level radioactive waste.

5.2 BUFFER REQUIREMENTS

The design concept of a vertical disposal system is shown in Figure 1. The disposal canister is emplaced in a deposition hole drilled from the floor of the disposal tunnel. The gap between the canister and wall of the deposition hole is filled with a buffer material. The buffer plays a role in protecting the waste and canister against any external mechanical impact, minimizing the inflow of groundwater from the surrounding rock, and restricting the release of nuclides contained in the waste.

The properties of the buffer material should be measured and characterized. In this regard, the requirements of the buffer, the characteristics of the domestic bentonite, and the thermal-hydro-mechanical properties of the candidate buffer material are described in this section. The major requirements for the buffer are as follows:

- Hydraulic conductivity: the hydraulic conductivity of the buffer material should be low enough to restrict the contact of groundwater from the surrounding rock with the disposal canister. The principal mechanism of radionuclide release through the buffer is diffusion.
- Sealing characteristics: the buffer material should have a high swelling property to fill the cracks of the host rock and the voids of the buffer when the repository is saturated with groundwater after its closure. On the other hand, the swelling pressure to the canister and the surrounding rock should be adequate so as not to change their external volumes without an excessive load.
- Thermal conductivity: the thermal conductivity of the buffer should be similar to that of the surrounding host rock.
- Mechanical properties: the buffer material should retain its mechanical strength to support the weight of the canister and the load of the surrounding rock, which should not cause any deformation or void space after the installation of the canister into a borehole. Also, cracks should not be produced by the elevation of the repository temperature or shrinkage of the buffer due to the decay heat.
- Radionuclide retention capacity: the buffer material should have a high distribution coefficient and low apparent diffusion coefficient to retard the release of radionuclides from the waste into the surrounding rock.
- Long-term integrity: the buffer material should keep its design performance for a certain period under the disposal environments and have its flexibility to accept any long-term deformation that would occur in the host rock.

The functional criteria are summarized in Table 1.

5.3 PROPERTIES OF BENTONITE BUFFER

Gyeongju bentonite is mostly Ca-type bentonite. Gyeongju bentonite consists of 70wt.% montmorillonite, 29wt.% feldspar, and about 1wt.% quartz (Figure 2). The chemical composition of Ca-bentonite is shown in Table 2. The bentonite mostly consists of SiO_2 and Al_2O_3. The amount of CaO in the bentonite is greater than that of Na_2O. The cation exchange capacity (CEC) of the buffer is 57.6 meq / 100 g. The specific gravity and surface area are 2.74 and 347.6 m_2/g, respectively. In addition, the liquid limit, plastic limit, and plasticity index of the buffer are 244.5%, 46.1% and 198.4%, respectively.

The properties of Ca-bentonite are investigated from the thermal, hydraulic, and mechanical point of view. The thermal conductivity of the Gyeongju bentonite is sensitive to the dry density and moisture content. As shown in Figure 3, the thermal conductivities of the bentonite blocks increase with an increase in the dry densities and moisture contents. The thermal conductivity according to the elevated moisture contents at each dry density of the buffers is expressed in the following equations:

$$k = 0.0378\,\omega_w - 0.0571 \left(\rho_d = 1.2\ Mg/m^3\right), \quad r^2 = 0.92 \tag{1}$$

$$k = 0.0681\,\omega_w - 0.2519 \left(\rho_d = 1.4\ Mg/m^3\right), \quad r^2 = 0.95 \tag{2}$$

$$k = 0.0599\,\omega_w - 0.0232 \left(\rho_d = 1.5\ Mg/m^3\right), \quad r^2 = 0.97 \tag{3}$$

$$k = 0.0640\,\omega_w - 0.0236 \left(\rho_d = 1.6\ Mg/m^3\right), \quad r^2 = 0.95 \tag{4}$$

$$k = 0.0574\,\omega_w - 0.2129 \left(\rho_d = 1.8\ Mg/m^3\right), \quad r^2 = 0.94 \tag{5}$$

where k is the thermal conductivity (W/mK), ω_w is the moisture content (wt.%), and ρ_d is the dry density (Mg/m_3).

The hydraulic conductivity of Gyeongju bentonite decreases with an increase of the dry density as shown in Figure 4, and is expressed as follows:

$$LogK = -4.07\rho_d - 6.13\ (at\ 20^\circ C) \quad r^2 = 0.92 \tag{6}$$

The hydraulic conductivity of Gyeongju bentonite increases with an increase in temperature. The hydraulic conductivity at 80°C is about 3-4 times greater than that at 20°C. The relative humidity of Gyeongju bentonite is measured using a humidity sensor, and the water potential (suction) is then determined using a Kelvin equation. As shown in Figure 5 and Figure 6, the water potential decreases with an increase in the water content at a constant temperature. These values show a

little difference compared with those of the bentonite powder. The water diffusion coefficient of bentonite block is determined using the diffusion model. The diffusion coefficients of Gyeongju bentonite blocks with their dry densities ranging from 1.4 to 1.8 Mg/m3 are 1.93×10^{-10} to 4.3×10^{-10} m^2/sec, and these values decrease with an increase in dry density.

The swelling pressure of Gyeongju bentonite blocks with dry densities of 1.4-1.8 Mg/m3 (non-activated with Na) is in the range of 0.4 to 9.5 MPa, and the swelling pressure increases with an increase in dry density. The uniaxial compressive strength, elastic modulus, and Poisson's ratio are determined by a uniaxial compression test. Table 3 shows the results of the uniaxial compression test for Gyeongju bentonite blocks.

The shear strength of the bentonite block was measured by a triaxial compression test method under an unconfined condition. The measured results are shown in Table 4. As shown in the table, the cohesion and internal friction angle increase with an increase in dry density. Consolidation characteristics are represented as a function of the coefficient of consolidation, Cv, coefficient of volume compressibility, mv, and compression index, Cc, and the values from the buffer are 0.018 m^2/yr, 0.02142 m^2/MN, and 0.14, respectively.

5.4 DESIGN OF BUFFER BLOCKS

The dry density of a buffer block is determined to be 1.6 Mg/m3. The porosity of the block is 0.41. Although 2 different kinds of deposition methods, horizontal and vertical, shown in Figure 7 and Figure 8, are proposed, a conceptual design of one buffer block set is carried out regardless of the deposition type.

Two kinds of buffer blocks, pineapple ring shaped blocks for the sides of the disposal canisters and disk shaped blocks for the bottoms and tops of the canisters, are used (Figure 9). The inner diameter and thickness of a pineapple ring shaped block are 105.0 cm and 36.0 cm, respectively. Twelve pineapple ring blocks 50 cm in height and two ring blocks 45 cm in height are emplaced around the four disposal canisters in a vertical borehole. The outer diameter and height of a disk shaped block are 177.0 cm and 50.0 cm, respectively. Seven disk blocks are emplaced in a borehole.

The compacted bentonite blocks are fabricated using the following procedure: drying and crushing raw bentonite ore, sieving these using a 200 mesh ASTM sieve, and compacting the sieved fine powder using a uniaxial hydraulic press to reach the target density. Thermal-hydro-mechanical properties of the reference buffer block are presented in Table 5 based on the experimental results.

Figure 1. Conceptual diagram of a reference disposal system.

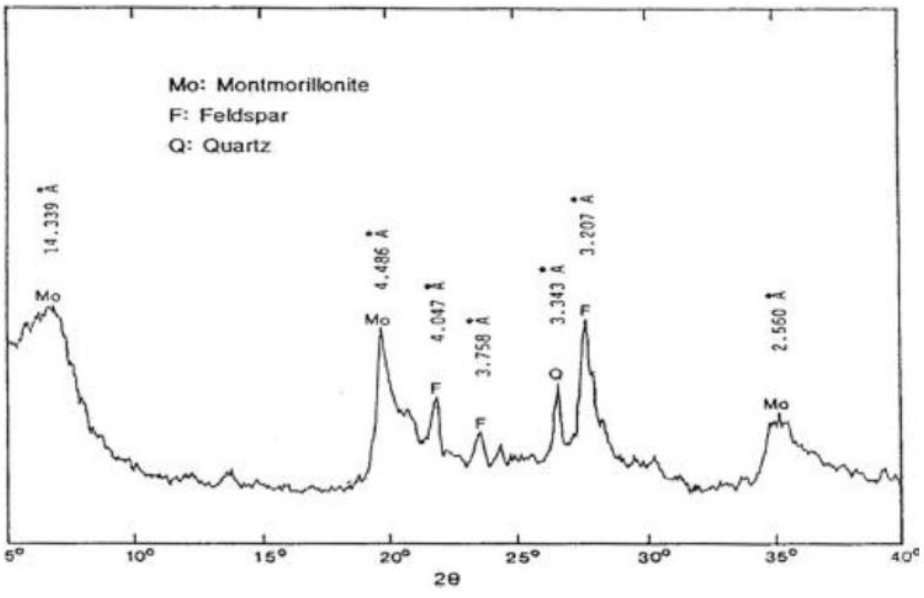

Figure 2. XRD pattern of Gyeongju bentonite.

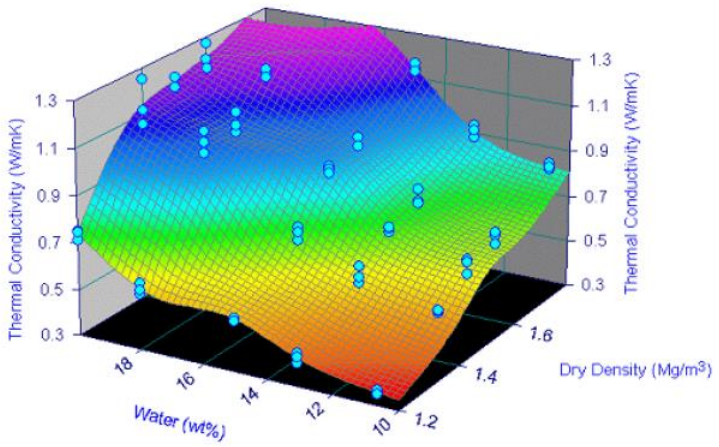

Figure 3. Change of the thermal conductivity of bentonite with respect to dry density and water content.

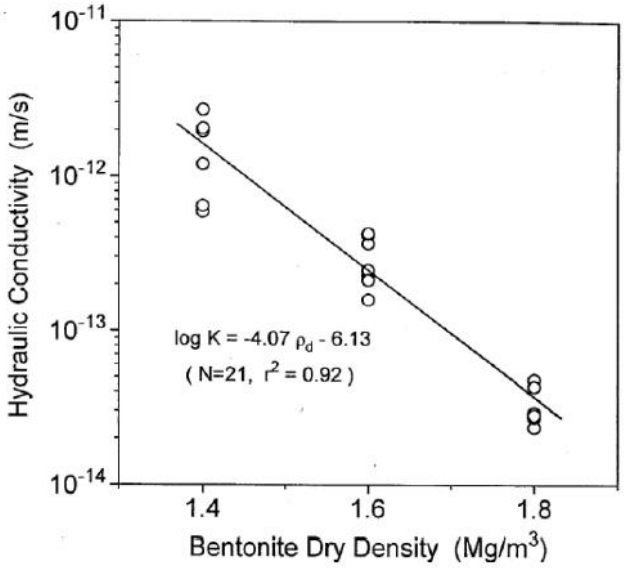

Figure 4. Hydraulic conductivity versus dry density for Gyeongju bentonite.

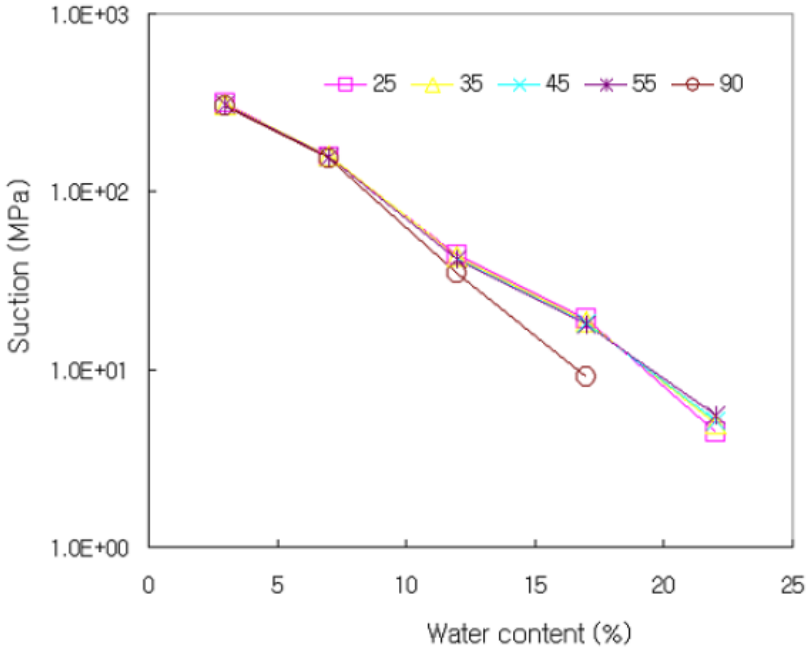

Figure 5. Suction versus water content relationship for different temperatures.

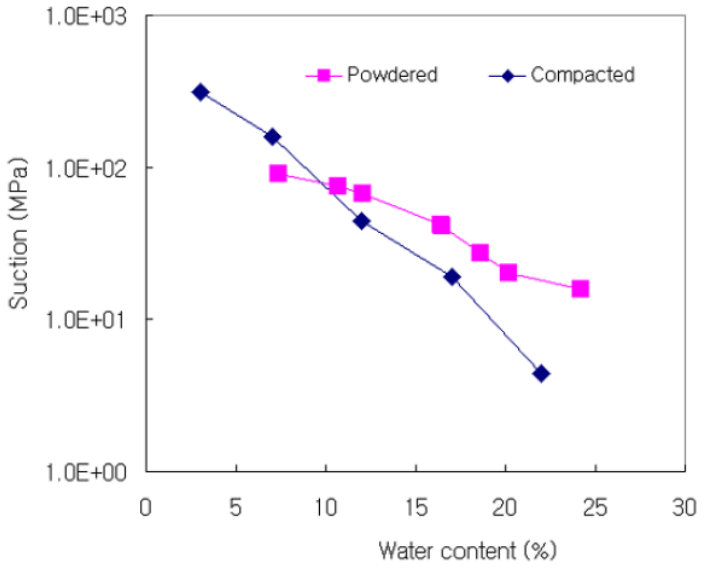

Figure 6. Comparison of suction-water content relationships between powder and compacted blocks.

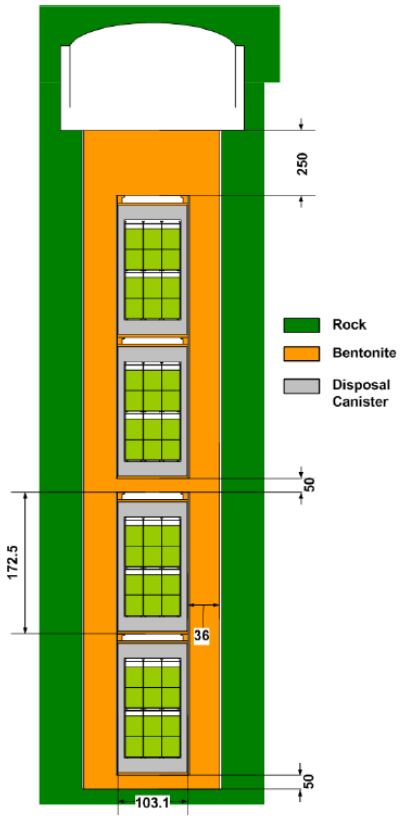

Figure 7. Schematic diagram of the buffer for a vertical deposition.

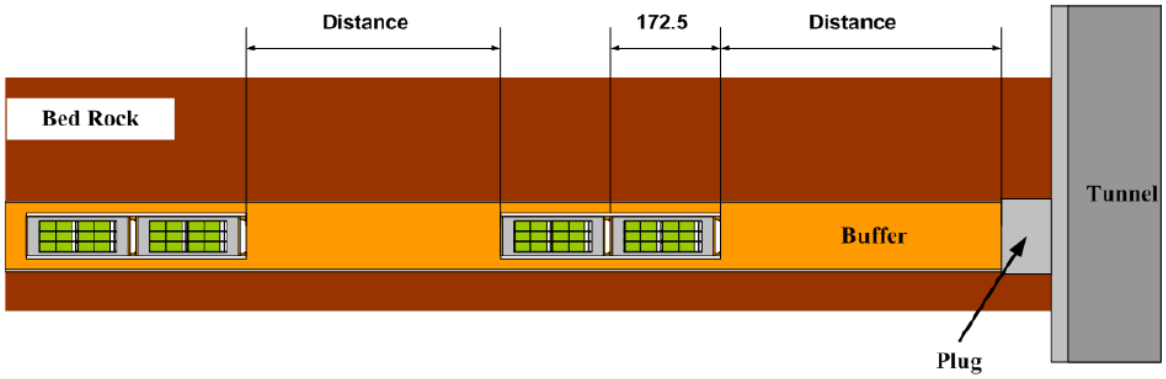

Figure 8. Schematic diagram of the buffer for a horizontal deposition.

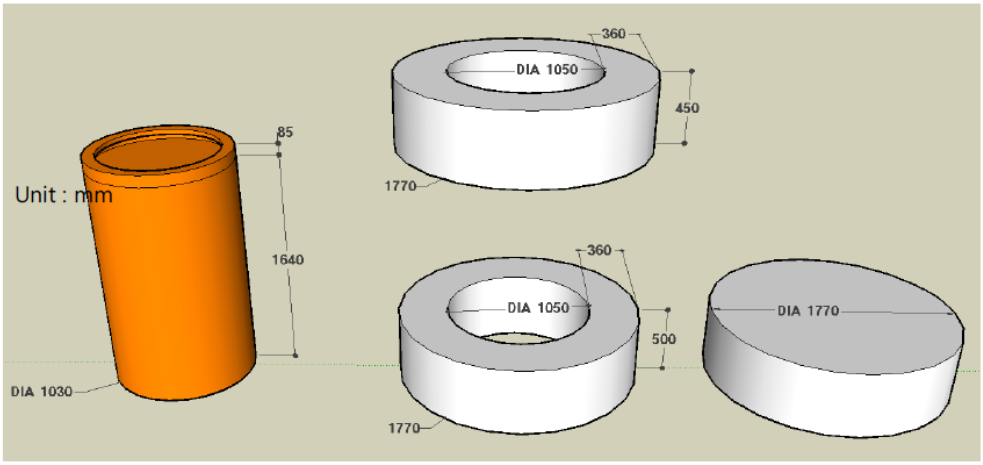

Figure 9. Design of the buffer blocks.

Table 1. Functional criteria of a buffer for the reference disposal system

Material Properties	Reference Value
Dry density (Mg/m^3)	≥ 1.6
Hydraulic conductivity (m/sec)	$< 10^{-12}$
Swelling pressure (MPa)	< 15.0
Mechanical properties	
- Unconfined compression strength (MPa)	> 4.9
- Young's modulus ($\times 10^2$ MPa)	≥ 5.9
- Poisson's ratio	0.05-0.21
- Cohesion (kPa)	500-1,000
- Internal friction angle (degree)	27-37
- Coefficient of consolidation (m^2/yr)	0.018-0.115
Thermal conductivity (W/mK)	≥ 0.8
Organic carbon content (wt.%)	< 0.3
Maximum temperature (°C)	< 100.0

Table 2. Chemical composition of Gyeongju bentonite

Chemical constituents	SiO_2	Al_2O_3	Fe_2O_3	CaO	MgO	K_2O	Na_2O	FeO	SO_3	MnO
wt.%	56.80	19.96	6.03	2.59	0.77	0.93	1.25	0.15	1.28	0.04

Table 3. Uniaxial compressive strength, elastic modulus, and Poisson ratio of bentonite blocks

Dry density (g/m^3)	Water content (%)	Unconfined compressive strength (MPa)	Young's modulus ($\times 10^2$ MPa)	Poisson's ratio
1.4	17.0	0.55	0.59	0.05
1.6	17.0	4.90	7.84	0.20
	17.0	4.90	5.88	0.18
1.8	17.0	7.84	10.79	0.21
	17.1	8.83	12.75	0.20

Table 4. Properties of shear strength (cohesion and friction angle) of bentonite blocks

Dry density (g/m^3)	Water content (%)	Cohesion (kPa)	Internal friction angle (degree)
1.4	17.0	500	27
1.6	17.0	1,000	37
1.8	17.0	1,100	50

Table 5. Thermo-hydro-mechanical properties of the reference buffer

Material Properties	Criteria	Values of Ca-bentonite
Dry density	≥ 1.6	1.6
Hydraulic conductivity	$< 10^{-12}$	3×10^{-13}
Swelling pressure (MPa)	< 15	7.0
Mechanical properties		
- Unconfined compression strength (MPa)	> 4.9	5.0
- Young's modulus ($\times10^2$ MPa)	≥ 5.9	5.9
- Poisson's ratio	0.05-0.21	0.18
- Cohesion (kPa)	500-1,000	1,000
- Internal friction angle (degree)	27-37	37
- Coefficient of consolidation (m^2/yr)	0.018-0.115	0.021
Thermal conductivity (W/mK)	≥ 0.8	0.8
Organic carbon content (wt.%)	< 0.3	

6. SUMMARY

The international collaboration on the evaluation of crystalline disposal media at SNL in FY15 was focused on the following four activities: (1) thermal-hydrologic-mechanical-chemical modeling single fracture evolution; (2) simulations of flow and transport in Bedrichov Tunnel, Czech Republic, (3) streaming potential testing at KAERI, and (4) technical data exchange with KAERI on THM properties and specifications of bentonite buffer materials. The first two activities are part of the DECOVALEX-2015 project. The major accomplishments include:

- *DECOVALEX C.1: Thermal-Hydrologic-Mechanical-Chemical (THMC) Processes in Single Fractures:* Understanding of subsurface fracture opening and closure is of great importance to oil/gas production, geothermal energy extraction, radioactive waste disposal, and carbon sequestration and storage. Fracture opening and closure involve a complex set of thermal, hydrologic, mechanical and chemical (THMC) processes. A fully coupled THMC model for fracture opening and closure is formulated by explicitly accounting for the stress concentration on aperture surface, stress-activated mineral dissolution, pressure solution at contacting asperities, and channel flow dynamics. A model analysis, together with reported laboratory observations, shows that a tangential surface stress created by a far-field compressive normal stress may play an important role in controlling fracture aperture evolution in a stressed geologic medium, a mechanism that has not been considered in any existing models. Based on the model analysis, a necessary condition for aperture opening has been derived. The model provides a reasonable explanation for many salient features of fracture evolution in laboratory experiments, including a spontaneous switch from a permeability reduction to a permeability increase in a static limestone experiment. The work may also help develop a new method for estimating in-situ stress in a reservoir.
- *DECOVALEX C.2: Bedrichov Tunnel Test Case:* The transit time distribution (TTD) of discharge collected from fractures in the Bedrichov Tunnel, Czech Republic, is investigated using lumped parameter models and multiple environmental tracers. We utilize time series of $\delta^{18}O$, $\delta^{2}H$ and $\delta^{3}H$ along with CFC measurements from individual fractures in the Bedrichov Tunnel of the Czech Republic to investigate the TTD, and the uncertainty in estimated mean travel time in several fracture networks of varying length and discharge. We compare several transit time distributions, including the dispersion distribution, the exponential distribution, and a developed TTD which includes the effects of matrix diffusion. The effect of seasonal recharge is explored by comparing several seasonal weighting functions to derive the historical recharge concentration. We identify best fit mean ages for each TTD by minimizing the error-weighted, multi-tracer χ^2 residual for each seasonal weighting function. We use this methodology to test the ability of each TTD and seasonal input function to fit the observed tracer concentrations, and the effect of choosing different TTD and seasonal recharge functions on the mean age estimation. We find that the estimated mean transit time is a function of both the assumed transit time distribution and seasonal weighting function. Best fits as measured by the χ^2 value were achieved for the dispersive model using the seasonal input function developed here for two of the three modeled sites, while at the third site, equally good fits were achieved with the exponential model and

the dispersion model and our seasonal input function. The average mean transit time for all TTDs and seasonal input functions converged to similar values at each location. The sensitivity of the estimated mean transit time to the seasonal weighting function was equal to that of the transit time distribution. These results indicated that understanding seasonality of recharge is at least as important as the uncertainty in the flow path distribution in fracture networks, and that unique identification of the TTD and mean transit time is difficult given the uncertainty in the recharge function. However, the mean transit time appears to be relatively robust to the structural model uncertainty. The results presented here should be applicable to other studies using environmental tracers to constrain ow and transport properties in fractured rock systems.

- *Collaboration with KAERI:* SNL and KAERI have developed a multi-year plan for joint field testing and modeling to support the study of high-level nuclear waste disposal in crystalline geologic media. In FY16, KAERI completed the task on streaming potential (SP) testing and initiated a new task on technique development for in-situ borehole characterization. The new task is a jointed effort between the UFD deep borehole disposal work package and the crystalline disposal R&D work package. In FY16, KAERI also provided the data on THM properties and specifications of bentonite buffer materials. For the streaming potential testing, a sandbox experiment was established at KAERI to study the hydroelectric coupling. An acrylic tank was filled up with homogeneous sand as a sand aquifer, and the upstream and downstream reservoirs were connected to the sand aquifer to control the hydraulic gradient. Under a steady-state water flow condition, a tracer test was performed in the sandbox with the help of peristaltic pump, and tracer samples were collected from the same interval of five screened wells in the sandbox. During the tracer test, SP signals resulting from the distribution of 20 nonpolarizable electrodes were measured at the top of the tank by a multichannel meter. The results showed that there were changes in the observed SP after injection of tracer, which indicated that the SP was likely to be related to the solute transport.

Future work will include: (1) developing a plan for the participation in the new phase of the DECOVALEX project, (2) initiating an actual field test at the KURT site for the development of in-situ measurement techniques in boreholes, and (3) using the data obtained from the international collaboration for UFD model validation and demonstration.